



1 Aerosol-radiation feedback deteriorates the wintertime haze in North China Plain

2

3 Jiarui Wu^{1,6}, Naifang Bei², Bo Hu³, Suixin Liu¹, Meng Zhou⁴, Qiyuan Wang¹, Xia Li^{1,6}, Lang Liu¹, Tian Feng¹,
4 Zirui Liu³, Yichen Wang¹, Junji Cao¹, Xuexi Tie¹, Jun Wang⁴, Luisa T. Molina⁵, and Guohui Li^{1*}

5

6 ¹Key Lab of Aerosol Chemistry and Physics, SKLLQG, Institute of Earth Environment, Chinese Academy of
7 Sciences, Xi'an, Shaanxi, China8 ²School of Human Settlements and Civil Engineering, Xi'an Jiaotong University, Xi'an, Shaanxi, China9 ³State Key Laboratory of Atmospheric Boundary Layer Physics and Atmospheric Chemistry, Institute of
10 Atmospheric Physics, Chinese Academy of Sciences, Beijing, 100029, China11 ⁴Department of Chemical and Biochemical Engineering & Interdisciplinary Graduate Program in
12 Geo-Informatics, University of Iowa, Iowa City, Iowa, USA13 ⁵Molina Center for Energy and the Environment, La Jolla, California, USA14 ⁶University of Chinese Academy of Science, Beijing, China15 *Correspondence to: Guohui Li (ligh@ieecas.cn)

16

17

18 **Abstract.** Atmospheric aerosols or fine particulate matters (PM_{2.5}) scatter or absorb a fraction
19 of the incoming solar radiation to cool or warm the atmosphere, decreasing surface
20 temperature and altering atmospheric stability to further affect the dispersion of air pollutants
21 in the planetary boundary layer (PBL). In the present study, simulations during a persistent
22 and heavy haze pollution episode from 05 December 2015 to 04 January 2016 in the North
23 China Plain (NCP) were performed using the WRF-CHEM model to comprehensively
24 quantify contributions of the aerosol shortwave radiative feedback (ARF) to near-surface
25 PM_{2.5} mass concentrations. The WRF-CHEM model generally performs well in simulating
26 the temporal variations and spatial distributions of air pollutants concentrations compared to
27 observations at ambient monitoring sites in NCP, and the simulated diurnal variations of
28 aerosol species are also consistent with the measurements in Beijing. Additionally, the model
29 simulates well the aerosol radiative properties, the downward shortwave flux, and the PBL
30 height against observations in NCP during the episode. During the episode, the ARF
31 deteriorates the haze pollution, increasing the near-surface PM_{2.5} concentration in NCP by
32 10.2 μg m⁻³ or with a contribution of 7.8% on average. Sensitivity studies have revealed that
33 high loadings of PM_{2.5} during the episode attenuate the incoming solar radiation down to the
34 surface, cooling the temperature of the low-level atmosphere to suppress development of
35 PBL and decrease the surface wind speed, further enhancing the relative humidity and
36 hindering the PM_{2.5} dispersion and consequently exacerbating the haze pollution in NCP. The
37 ensemble analysis indicates that when the near-surface PM_{2.5} mass concentration increases
38 from around 50 to several hundred μg m⁻³, the ARF contributes to the near-surface PM_{2.5} by
39 more than 20% during daytime in NCP, substantially aggravating the heavy haze formation.
40 However, when the near-surface PM_{2.5} concentration is less than around 50 μg m⁻³, the ARF



41 generally reduces the near-surface $PM_{2.5}$ concentration due to the consequent perturbation of
42 atmospheric dynamic fields.

43

44

45

46

47



48 1 Introduction

49 Atmospheric aerosols, produced both naturally and anthropogenically, influence the
50 radiative energy budget of the Earth's atmospheric system in many ways. They scatter or
51 absorb a fraction of the incoming solar radiation to cool or warm the atmosphere, decreasing
52 surface temperature and altering atmospheric stability (e.g., Ackerman, 1977; Jacobson, 1998,
53 2002). Also, they serve as cloud condensation nuclei (CCN) and ice nuclei (IN), thus
54 modifying cloud optical properties and lifetime (e.g., Zhang et al., 2007; Li et al., 2008;
55 2009). Among those impacts, the scattering and absorption of solar radiation by aerosols and
56 the associated feedbacks (hereafter referred to as aerosol-radiation feedback or ARF) not only
57 constitute one of the main uncertainties in climate prediction (IPCC, 2007), but also
58 substantially affect the atmospheric chemistry by perturbing the temperature profile and
59 moistures, winds, and planetary boundary layer (PBL) stability (Boucher et al., 2013).
60 Particularly, as a short-lived pollutant with uneven distribution and physical and chemical
61 heterogeneities in the atmosphere, the ARF varies by more than a factor of ten with location
62 or time of emissions (Penner et al., 2010).

63 During wildfire with high loading absorbing aerosols, the ARF has been reported to heat
64 the atmosphere and cool the surface, and thence enhance the PBL stability (e.g., Grell et al.,
65 2011; Fu et al., 2012; Wong et al., 2012). In addition, numerous studies have been performed
66 to evaluate impacts of the ARF of dust on the regional meteorology and climate (e.g., Perez et
67 al., 2006; D. Zhang et al., 2009; Santese et al., 2010). Anthropogenic aerosols, dominated by
68 scattering components, such as organics and sulfate, primarily attenuate the incoming solar
69 radiation down to the surface, cooling the temperature of the low-level atmosphere to
70 suppress the development of PBL and hinder the aerosol dispersion in the vertical direction
71 (e.g., Fast et al., 2006; Vogel et al., 2009; Zhang et al., 2010). In addition, the temperature
72 profile perturbation caused by the ARF also alters cloud formation and development, possibly



73 causing the precipitation delay or decrease (e.g., Zhao et al., 2005; Koch and Del Genio, 2010;
74 Ding et al., 2013).

75 Rapid industrialization and urbanization in China have significantly elevated the
76 concentrations of aerosols or fine particulate matters (PM_{2.5}), causing frequent occurrence of
77 haze pollution, particularly during wintertime in North China (e.g., Zhang et al., 2013; Pui et
78 al., 2014). Guo et al. (2014) have elucidated the haze formation mechanism in China,
79 highlighting the efficient aerosol nucleation and growth during haze episodes. Moreover, high
80 loading aerosols during heavy haze episodes induce efficient ARF, encumbering the PBL
81 development and further deteriorating the haze pollution. It is worth noting that the ARF
82 increases precursors for the aerosol nucleation and growth in the PBL, such as sulfuric and
83 organic gases, causing efficient aerosol nucleation and growth (Zhang et al., 2004; Guo et al.,
84 2014). Based on field measurements, recent studies have proposed that the high level of
85 PM_{2.5} increases the stability of PBL due to the ARF and further decrease the PBL height
86 (PBLH), consequently enhancing PM_{2.5} concentrations ([PM_{2.5}]) (Quan et al., 2013; Petaja et
87 al., 2016; Yang et al., 2016; Tie et al., 2017; Ding et al., 2017). Online-coupled meteorology
88 and chemistry models have also been used to verify the impact of the ARF on the PBLH and
89 near-surface [PM_{2.5}] during heavy haze episodes in North China (Z. Wang et al., 2014; Wang
90 et al., 2015; Zhang et al., 2015; Gao et al., 2015). However, the ARF impact on near-surface
91 [PM_{2.5}] varies, depending on the evaluation time and location (Table 1). For example, the
92 two-way coupled WRF-CMAQ system has been employed to evaluate the ARF contribution
93 to the haze formation in January 2013 over the North China Plain (NCP), showing that the
94 ARF reduces the PBLH by 100 m and enhances near-surface [PM_{2.5}] by up to 140 μg m⁻³ in
95 Beijing (J. Wang et al., 2014). Therefore, it is still imperative to comprehensively quantify the
96 ARF contribution to near-surface [PM_{2.5}] under various pollution levels to provide the
97 underlying basis for supporting the design and implementation of emission control strategies.



98 In this study, simulations are performed using the Weather Research and Forecast model
99 with Chemistry (WRF-CHEM) to interpret the relationship between the near-surface [PM_{2.5}]
100 and the PBLH and further quantify the ARF contribution to near-surface [PM_{2.5}] under
101 various pollution levels. The model and methodology are described in Section 2. Analysis
102 results and discussions are presented in Section 3, and summary and conclusions are given in
103 Section 4.

104 2 Model and methodology

105 2.1 WRF-CHEM model and configurations

106 The WRF-CHEM model (Grell et al., 2005) with modifications by Li et al. (2010, 2011a,
107 b, 2012) is applied to evaluate effects of the ARF on the wintertime haze formation in NCP.
108 The model includes a new flexible gas phase chemical module and the CMAQ aerosol
109 module developed by US EPA (Binkowski and Roselle, 2003). The wet deposition is based
110 on the method in the CMAQ module and the dry deposition of chemical species follows
111 Wesely (1989). The photolysis rates are calculated using the FTUV (fast radiation transfer
112 model) with the aerosol and cloud effects on photolysis (Li et al., 2005, 2011a). The
113 inorganic aerosols are predicted using ISORROPIA Version 1.7, calculating the composition
114 and phase state of an ammonium-sulfate-nitrate-water inorganic aerosol in thermodynamic
115 equilibrium with gas phase precursors in the study (Nenes, 1998). The secondary organic
116 aerosol (SOA) is calculated using the volatility basis-set (VBS) modeling method, with
117 contributions from glyoxal and methylglyoxal. Detailed information can be found in Li et al.
118 (2010, 2011b).

119 A persistent air pollution episode from 05 December 2015 to 04 January 2016 in NCP is
120 simulated using the WRF-CHEM model. Figure 1a shows the model simulation domain, and
121 detailed model configurations can be found in Table 2.

122 2.2 Aerosol radiative module



123 In the present study, Goddard shortwave module developed by Chou and Suarez (1999,
 124 2001) is employed to take into account the ARF effect on the haze formation. The aerosol
 125 radiative module developed by Li et al. (2011b) has been incorporated into the WRF-CHEM
 126 model to calculate the aerosol optical depth (AOD or τ_a), single scattering albedo (SSA or
 127 ω_a), and the asymmetry factor (g_a).

128 In the CMAQ aerosol module, aerosols are represented by a three-moment approach
 129 with a lognormal size distribution:

$$130 \quad n(\ln D) = \frac{N}{\sqrt{2\pi} \ln \sigma_g} \exp\left[-\frac{1}{2} \left(\frac{\ln D - \ln D_g}{\ln \sigma_g}\right)^2\right] \quad (1)$$

131 Where D is the particle diameter, N is the number distribution of all particles in the
 132 distribution, D_g is the geometric mean diameter, and σ_g is the geometric standard deviation.

133 To calculate the aerosol optical properties, the aerosol spectrum is first divided into 48 bins
 134 from 0.002 to 2.5 μm , with radius r_i . The aerosols are classified into four types: (1)
 135 internally mixed sulfate, nitrate, ammonium, hydrophilic organics and black carbon, and
 136 water; (2) hydrophobic organics; (3) hydrophobic black carbon; and (4) other unidentified
 137 aerosols. These four kinds of aerosols are assumed to be mixed externally. For the internally
 138 mixed aerosols, the complex refractive index at a certain wavelength (λ) is calculated based
 139 on the volume-weighted average of the individual refractive index. Given the particle size
 140 and complex refractive index, the extinction efficiency (Q_e), ω_a and g_a are calculated
 141 using the Mie theory at a certain wavelength (λ). The look-up tables of Q_e , ω_a and g_a are
 142 established according to particle sizes and refractive indices to avoid multiple Mie scattering
 143 calculation. The aerosol optical parameters are interpolated linearly from the look-up tables
 144 with the calculated refractive index and particle size in the module.

145 The aerosol optical depth (AOD or τ_a) at a certain wavelength (λ) in a given
 146 atmospheric layer k is determined by the summation over all types of aerosols and all bins:

$$147 \quad \tau_a(\lambda, k) = \sum_{i=1}^{48} \sum_{j=1}^4 Q_e(\lambda, r_i, j, k) \pi r_i^2 n(r_i, j, k) \Delta Z_k \quad (2)$$



148 where $n(\mathbf{r}_i, \mathbf{j}, \mathbf{k})$ is the number concentration of \mathbf{j} -th kind of aerosols in the i -th bin. ΔZ_k is
 149 the depth of an atmospheric layer. The weighted-mean values of σ and \mathbf{g} are then
 150 calculated by (d'Almeida et al., 1991):

$$151 \quad \omega_a(\lambda, \mathbf{k}) = \frac{\sum_{i=1}^{48} \sum_{j=1}^4 Q_e(\lambda, \mathbf{r}_i, \mathbf{j}, \mathbf{k}) \pi r_i^2 n(\mathbf{r}_i, \mathbf{j}, \mathbf{k}) \omega_a(\mathbf{r}_i, \mathbf{j}, \mathbf{k}) \Delta Z_k}{\sum_{i=1}^{48} \sum_{j=1}^4 Q_e(\lambda, \mathbf{r}_i, \mathbf{j}, \mathbf{k}) \pi r_i^2 n(\mathbf{r}_i, \mathbf{j}, \mathbf{k}) \Delta Z_k} \quad (3)$$

$$152 \quad \mathbf{g}_a(\lambda, \mathbf{k}) = \frac{\sum_{i=1}^{48} \sum_{j=1}^4 Q_e(\lambda, \mathbf{r}_i, \mathbf{j}, \mathbf{k}) \pi r_i^2 n(\mathbf{r}_i, \mathbf{j}, \mathbf{k}) \omega_a(\mathbf{r}_i, \mathbf{j}, \mathbf{k}) \mathbf{g}_a(\lambda, \mathbf{r}_i, \mathbf{j}, \mathbf{k}) \Delta Z_k}{\sum_{i=1}^{48} \sum_{j=1}^4 Q_e(\lambda, \mathbf{r}_i, \mathbf{j}, \mathbf{k}) \pi r_i^2 n(\mathbf{r}_i, \mathbf{j}, \mathbf{k}) \omega_a(\mathbf{r}_i, \mathbf{j}, \mathbf{k}) \Delta Z_k} \quad (4)$$

153 When the wavelength-dependent τ_a , ω_a , and \mathbf{g}_a are calculated, they can be used in the
 154 Goddard shortwave module to evaluate the ARF. Detailed information can be found in Li et
 155 al. (2011b).

156 2.3 Data and statistical methods for comparisons

157 The model performance is validated using the available measurements in NCP, including
 158 AOD, SSA, PBLH, downward shortwave flux (SWDOWN), aerosol species, and air
 159 pollutants. The daily AOD is retrieved from Terra- and Aqua- Moderate Resolution Imaging
 160 Spectroradiometer (MODIS) level 2 products, with a resolution of $0.1^\circ \times 0.1^\circ$. The hourly SSA
 161 is calculated using the measurement of the turbidity meter at the National Center for
 162 Nanoscience and Technology (NCNST), Chinese Academy of Sciences (116.33°E , 39.99°N)
 163 in Beijing (Figure 1b). The daily PBLH at 12:00 Beijing time (BJT) is diagnosed from the
 164 radiosonde observation at a meteorological site (116.47°E , 39.81°N) in Beijing. The
 165 SWDOWN is measured by CM-11 pyranometers at four sites from Chinese Ecosystem
 166 Research Network (CERN) in NCP (Liu et al., 2016). The hourly measurements of O_3 , NO_2 ,
 167 SO_2 , CO and $\text{PM}_{2.5}$ concentrations have been released by the China's Ministry of Ecology
 168 and Environment (China MEP) since 2013. The hourly submicron sulfate, nitrate, ammonium,
 169 and organic aerosols are measured by the Aerodyne Aerosol Chemical Speciation Monitor
 170 (ACSM) at NCNST. The primary organic aerosol (POA) and SOA concentrations are
 171 obtained from the ACSM measurement analyzed using the Positive Matrix Factorization



172 (PMF). In addition, we have also analyzed the relationship between near-surface [PM_{2.5}] and
173 the PBLH retrieved from the Lidar measurement at the Institute of Remote Sensing and
174 Digital Earth (IRSDE), Chinese Academy of Sciences (116.38°E, 40.00°N) in Beijing (Figure
175 1b).

176 In the present study, the mean bias (*MB*), root mean square error (*RMSE*) and the index
177 of agreement (*IOA*) are used to assess the performance of WRF-CHEM model simulations
178 against measurements. *IOA* describes the relative difference between the model and
179 observation, ranging from 0 to 1, with 1 indicating perfect agreement.

$$180 \quad MB = \frac{1}{N} \sum_{i=1}^N (P_i - O_i) \quad (5)$$

$$181 \quad RMSE = \left[\frac{1}{N} \sum_{i=1}^N (P_i - O_i)^2 \right]^{\frac{1}{2}} \quad (6)$$

$$182 \quad IOA = 1 - \frac{\sum_{i=1}^N (P_i - O_i)^2}{\sum_{i=1}^N (|P_i - \bar{P}| + |O_i - \bar{O}|)^2} \quad (7)$$

183 Where P_i and O_i are the predicted and observed value of a variable, respectively. N is the
184 total number of the predictions used for comparisons, and \bar{P} and \bar{O} represents the average
185 of the prediction and observation, respectively.

186

187 3 Results and discussions

188 3.1 Model performance

189 We first define the base simulation in which the ARF is considered (hereafter referred to
190 as f_{base}), and results from f_{base} are compared to observations in NCP.

191 3.1.1 Air pollutants simulations in NCP

192 Figure 2 shows the spatial pattern of calculated and observed average near-surface
193 concentrations of PM_{2.5}, O₃, NO₂, and SO₂ along with simulated winds from 05 December
194 2015 to 04 January 2016 in Eastern China. In general, the simulated air pollutants
195 distributions are in good agreement with the measurements, but model biases still exist. The



196 simulated winds are weak or calm during the simulation period, facilitating accumulation of
197 air pollutants and causing the serious air pollution in Eastern China. NCP is the most polluted
198 region due to its massive air pollutants emissions, with the average near-surface $[PM_{2.5}]$
199 generally exceeding $115 \mu\text{g m}^{-3}$. The highest average near-surface $[PM_{2.5}]$ of more than 150
200 $\mu\text{g m}^{-3}$ are observed in Beijing, Hebei, Henan, Shandong, and the Guanzhong basin, which
201 are well reproduced by the model. The simulated O_3 concentrations are rather low in NCP,
202 ranging from 5 to $40 \mu\text{g m}^{-3}$, consistent with measurements. The low O_3 concentration during
203 wintertime haze episodes in NCP is primarily caused by the weak insolation further
204 attenuated by clouds and aerosols, the titration of high NO_x emissions, and lack of the O_3
205 transport from outside (Li et al., 2018). Although significant effort has been made to mitigate
206 air pollutants emissions in NCP, the observed and simulated average NO_2 and SO_2
207 concentrations are still high, varying from 30 to $100 \mu\text{g m}^{-3}$ and 20 to $100 \mu\text{g m}^{-3}$,
208 respectively. Interestingly, the simulated high SO_2 concentrations are mainly concentrated in
209 cities and their surrounding areas, but the uniform distribution of NO_2 concentrations is
210 predicted in NCP, showing the substantial contribution of area sources.

211 Figure 3 shows the temporal profiles of observed and calculated near-surface $PM_{2.5}$, O_3 ,
212 NO_2 , SO_2 and CO concentrations averaged over monitoring sites in NCP from 05 December
213 2015 to 04 January 2016. The model generally tracks well the diurnal variation of
214 near-surface $[PM_{2.5}]$ in NCP, with *IOA* of 0.94, but slightly overestimates $[PM_{2.5}]$, with a *MB*
215 of $8.3 \mu\text{g m}^{-3}$. The model successfully reproduces the temporal variations of near-surface O_3
216 concentrations compared to observations in NCP, e.g., peak O_3 concentrations in the
217 afternoon due to active photochemistry and low O_3 concentrations during nighttime caused
218 by the NO_x titration, with an *IOA* of 0.94. However, the model generally underestimates the
219 O_3 concentration during nighttime, with a *MB* of $-3.6 \mu\text{g m}^{-3}$. The model also reasonably well
220 yields the NO_2 diurnal profiles with peaks in the evening, with an *IOA* of 0.86 and a *MB* of



221 $1.6 \mu\text{g m}^{-3}$, but sometimes there are considerable overestimations and underestimations. The
222 model generally performs reasonably in predicting the temporal variation of SO_2
223 concentrations against measurements, with an *IOA* of 0.74. However, considering that SO_2 is
224 mainly emitted from point sources and its simulations are more sensitive to the wind field
225 uncertainties (Bei et al., 2017), the overestimation and underestimation for the SO_2
226 simulation is rather large, with a *RMSE* of $13.3 \mu\text{g m}^{-3}$. Compared with measurements, the
227 temporal profile of the near-surface CO concentration in NCP is well simulated, with the *IOA*
228 and *MB* of 0.87 and $0.1 \mu\text{g m}^{-3}$, respectively.

229 3.1.2 Aerosol species simulations in Beijing

230 Figure 4 provides the temporal variations of simulated and observed aerosol species at
231 NCNST in Beijing from 05 December 2015 to 04 January 2016. Generally, the WRF-CHEM
232 model predicts reasonably the temporal variations of the aerosol species against the
233 measurements. The WRF-CHEM model yields the main peaks of the POA concentration
234 compared to observations in Beijing, but frequently underestimates or overestimates the POA
235 concentration, with an *IOA* of 0.80 and a *RMSE* of $17.4 \mu\text{g m}^{-3}$. The POA level in Beijing is
236 influenced by local emissions and to a large extent trans-boundary transport from outside
237 during haze days, so its simulation is sensitive to uncertainties from emissions and
238 meteorological fields (Bei et al., 2010, 2012). The model still has difficulties in simulating
239 the SOA concentrations, although the VBS modeling method is used and contributions from
240 glyoxal and methylglyoxal are included in the study, with *IOA* and *MB* of 0.77 and $-10.6 \mu\text{g}$
241 m^{-3} , respectively. Except the SOA formation and transformation mechanism in the
242 atmosphere, which remains elusive, many factors have potentials to influence the SOA
243 simulation, such as meteorology, measurements, precursors emissions, and SOA treatments
244 (Li et al., 2011a). The model reasonably tracks the temporal variation of the observed sulfate
245 concentration, and the *MB* and *IOA* are $0.6 \mu\text{g m}^{-3}$ and 0.90, respectively. Aside from SO_2



246 emissions and simulated meteorological fields, the SO₂ oxidation mechanism in the
247 atmosphere also plays an important role in the sulfate simulation. In addition to direct
248 emissions and SO₂ gas-phase oxidations by hydroxyl radicals (OH) and stabilized criegee
249 intermediates (sCI), the SO₂ oxidation in aerosol water by O₂ catalyzed by Fe³⁺ is considered
250 (Li et al., 2017a). Recent studies have proposed that the aqueous oxidation of SO₂ by NO₂
251 under the condition of high RH and NH₃ neutralization could interpret the efficient sulfate
252 formation during wintertime haze events (Wang et al., 2016; Cheng et al., 2016). However,
253 the mechanism is still not included in this study, which might further improve the sulfate
254 simulation. The model performs well in simulating the nitrate and ammonium concentrations
255 against observations in Beijing, with *IOAs* of 0.90 and 0.91, respectively.

256 3.1.3 Aerosol radiative properties simulations in NCP

257 Aerosol radiative forcing mainly depends on AOD, SSA, and asymmetry parameter (*g*).
258 The model validations of AOD and SSA are provided in this study to further evaluate the
259 aerosol radiative effect on the air pollution. The daily AOD at 550 nm, retrieved from Terra-
260 and Aqua- MODIS level 2 products, is compared with the simulation. Figure 5a shows the
261 scatter plot of the daily retrieved and simulated AOD averaged in NCP from 05 December
262 2015 to 04 January 2016. The simulated daily average AOD correlates well with the
263 observation, with a correlation coefficient of 0.86. Generally, the retrieved and simulated
264 AOD increases with deterioration of the haze pollution, but the model considerably
265 underestimates the AOD against the observation. Figure 5b presents the Taylor diagram
266 (Taylor, 2001) to show the variance, bias and correlation of the simulated and retrieved AOD
267 from 05 December 2015 to 04 January 2016. There exists a good relationship between the
268 simulated and retrieved daily AOD during the study episode, with correlation coefficients
269 generally ranging from 0.5 to 0.9, and standard deviation mostly varying from 0.25 to 1.0.
270 Figure 6 shows the pattern comparison of the retrieved and simulated AOD averaged during



271 the simulation period. The model reasonably reproduces the AOD distribution compared to
272 the observations in NCP, but considerably underestimates the AOD. The simulated and
273 retrieved AOD averaged in NCP during the simulation period is 0.43 and 0.59, respectively. It
274 is worth noting that the simulated AOD is not only dependent on the column aerosol content
275 and constituent, but is also significantly influenced by the relative humidity (RH) controlling
276 the aerosol hygroscopic growth. Additionally, the satellite retrieved AOD is subject to
277 contamination by existence of clouds, and considering the high occurrence frequency of
278 clouds during haze days, the retrieved AOD is generally higher than the simulation
279 (Engstrom and Ekman, 2010; Chand et al., 2012; Grandey et al., 2013).

280 Aerosols are the mixture of absorbing and scattering constituents in the atmosphere.
281 Their radiative effect of cooling or warming the atmosphere relies on many parameters, and
282 SSA is one of the most important (Satheesh et al., 2010). Figure 7 depicts the comparison of
283 the measured and simulated diurnal profiles of SSA at NCNST in Beijing during the episodes.
284 The model performs reasonably in simulating the daily variation of SSA in Beijing, with an
285 *IOA* of 0.69 and a *MB* of 0.0, but the overestimation or underestimation is rather large. SSA is
286 the ratio of scattering to extinction, which is highly sensitive to the relative distribution of
287 scattering and absorbing aerosol constituents in the atmosphere, and the RH determining the
288 hygroscopic growth of aerosols. Therefore, the uncertainties of the simulated SSA probably
289 originated from the model biases of aerosol constituents and the RH.

290 3.1.4 Downward solar radiation simulations in North China Plain

291 Figure 8 presents the daily profiles of simulated and observed SWDOWN at ground
292 surfaces in Beijing, Jiaozhouwan, Luancheng, and Yuancheng from 05 December 2015 to 04
293 January 2016. The WRF-CHEM model simulates well the daily variation of SWDOWN,
294 especially in Jiaozhouwan, Luancheng, and Yucheng, with *IOAs* around 0.90. The model is
295 subject to overestimating the SWDOWN against measurements, with *MBs* ranging from 6.3



296 to 86.2 W m^{-2} . The SWDOWN reaching the ground surface is very sensitive to the cloud
297 cover and optical thickness. However, the WRF-CHEM model still has difficulties in
298 accurately predicting the cloud cover and optical thickness, which might constitute one of the
299 most important reasons for model biases of the SWDOWN. In addition, the horizontal
300 resolution used in simulations cannot adequately resolve the cumulus clouds, also causing
301 uncertainties in the simulations of the SWDOWN.

302 3.1.5 PBLH simulations in Beijing

303 Figure 9 shows the temporal variations of the observed and simulated PBLH at a
304 meteorological site in Beijing from 05 December 2015 to 04 January 2016. The average
305 PBLH at 12:00 BJT during the episode at the meteorological site is 465.2 m, with the
306 minimum of 101.8 m and the maximum of 1017.9 m, showing decreased PBLH during the
307 haze episode. In general, the WRF-CHEM model tracks reasonably the daily variation of the
308 PBLH in Beijing, with an *IOA* of 0.70. However, the model has difficulties in reproducing the
309 observed very low PBLH, e.g., less than 200 m. The PBLH varies substantially with time due
310 to many factors including large-scale dynamics, cloudiness, convective mixing, and the
311 diurnal cycle of solar radiation (Sivaraman et al., 2013). Therefore, the simulation
312 uncertainties of meteorological conditions constitute the main reason for the simulation bias
313 of PBLH. For example, the overestimation of SWDOWN at 12:00 BJT (Figure 8a) probably
314 caused the overestimation of PBLH in Beijing.

315 In general, the simulated variations of SWDOWN, PBLH, aerosol radiative properties,
316 air pollutants ($\text{PM}_{2.5}$, O_3 , NO_2 , SO_2 , CO) and aerosol species are in good agreement with
317 observations, indicating that the simulations of meteorological conditions, chemical processes
318 and the emission inventory used in the WRF-CHEM model are reasonable, providing a
319 reliable basis for the further investigation.

320 3.2 Relationship between near-surface [$\text{PM}_{2.5}$] and PBLH



321 Figure 10 presents the scatter plot of the Lidar retrieved PBLH at IRSDE and
322 near-surface $[PM_{2.5}]$ at a monitoring site close to IRSDE during daytime (08:00 ~ 17:00 LT)
323 from 08 January to 20 February 2014. The wind speeds (WSPD) at a meteorological site
324 close to IRSDE are shown by the color of the filled circles in Figure 10. Additionally,
325 near-surface $[PM_{2.5}]$ during daytime are also subdivided into 20 bins with the interval of 25
326 $\mu\text{g m}^{-3}$. The PBLH as the bin of near-surface $[PM_{2.5}]$ is assembled, and an average of PBLH
327 in each bin is calculated (Nakajima et al., 2001; Kawamoto et al., 2006), which is represented
328 by the rectangle in Figure 10. Generally, on average, when the PBLH decreases from 1500 m
329 to around 400 m, the near-surface $[PM_{2.5}]$ increase from 10 to more than 200 $\mu\text{g m}^{-3}$. When
330 near-surface $[PM_{2.5}]$ exceed 200 $\mu\text{g m}^{-3}$, the PBLH remains 400~500 m. Previous studies
331 have also reported the nonlinear relationship between the PBLH and near-surface $[PM_{2.5}]$,
332 and proposed that increasing $[PM_{2.5}]$ reduce the PBLH or the ARF is attributed to the PBLH
333 decrease (e.g., Petaja et al., 2016; Tie et al., 2017; Liu et al., 2018).

334 The PBLH is primarily determined by the wind shear in the vertical direction and the
335 thermal condition of ground surfaces. The occurrence of low near-surface $[PM_{2.5}]$ generally
336 corresponds to efficient dispersions of $PM_{2.5}$ in horizontal and/or vertical directions. The
337 strong horizontal winds in the lower atmosphere not only disperse $PM_{2.5}$ emitted or formed
338 efficiently, but also intensify the wind shear in the vertical direction, increasing the PBLH
339 and facilitating the rapid vertical exchange of $PM_{2.5}$ in the PBL. When near-surface $[PM_{2.5}]$
340 are less than 50 $\mu\text{g m}^{-3}$, the PBLH exceeding 1000 m is observed, which is chiefly
341 determined by strong horizontal winds and less influenced by the ground thermal condition
342 during wintertime, and the observed average WSPD is about 2.4 m s^{-1} . The occurrence of
343 high near-surface $[PM_{2.5}]$ indicates that the lower atmosphere is stable or stagnant, with weak
344 horizontal winds and inactive convections, hindering the dispersion of $PM_{2.5}$ in the horizontal
345 and vertical directions. Additionally, as the horizontal winds become weak or calm, the wind



346 shear in the vertical direction is diminished and the PBLH is dominated by the ground
347 thermal condition. When near-surface $[PM_{2.5}]$ increase from 50 to around $200 \mu\text{g m}^{-3}$, the
348 PBLH decreases from around 700 to 400 m, and the average WSPD decreases to 1.8 m s^{-1} .
349 However, the increased $PM_{2.5}$ reducing PBLH still cannot be fully attributed to the ARF,
350 which is more likely caused by the decrease of winds or the formation of stagnant situations
351 in the low-level atmosphere. When near-surface $[PM_{2.5}]$ exceed $200 \mu\text{g m}^{-3}$, the observed
352 PBLH fluctuates between 400 and 500 m with the average WSPD of around 1.0 m s^{-1} , and
353 does not exhibit continuous decrease with the increasing near-surface $[PM_{2.5}]$.

354 Under the stagnant situation with weak winds, the PBLH is more sensitive to the ground
355 thermal condition. Increasing aerosols or $PM_{2.5}$ in the low-level atmosphere attenuate the
356 SWDOWN to the ground surface and decrease the surface temperature (TSFC) and
357 turbulence kinetic energy, suppressing the PBL development and further enhancing
358 near-surface $[PM_{2.5}]$. Therefore, with near-surface $[PM_{2.5}]$ exceeding $200 \mu\text{g m}^{-3}$, the inert
359 PBLH might be caused by the defect of the Lidar retrieved PBLH. The aerosol backscatter
360 signal received by Lidar is used to retrieve the PBLH. If the atmosphere is stable, the aerosols
361 near the maximal PBLH are subject to being confined in situ, and the retrieved PBLH is
362 generally the maximal one. Additionally, it is worth noting that the occurrence of the
363 wintertime severe haze pollution in NCP is often accompanied with the high-level
364 convergence between 500 and 700 hPa, producing a persistent and strong sinking motion in
365 the mid-lower troposphere to reduce the PBLH and facilitate accumulation of air pollutants
366 (Wu et al. 2017; Ding et al., 2017). Therefore, a subsidence inversion appears in the lower
367 layer as a result of the air masses sinking in the middle-troposphere, restraining the PBL
368 development and determining the maximal PBLH. Hence, it is imperative to evaluate the
369 ARF to the PBLH and near-surface $[PM_{2.5}]$.

370 3.3 Sensitivity studies



371 The conceptual model about the ARF contribution to the heavy haze formation has been
372 established in previous studies (e.g., Tie et al., 2017; Liu et al., 2018). During wintertime,
373 under stagnant meteorological situations with weak winds and humid air, air pollutants are
374 subject to accumulation in the PBL, facilitating the formation of PM_{2.5}. Increasing PM_{2.5} in
375 the PBL absorbs or scatters the incoming solar radiation to decrease the TSFC and facilitate
376 anomalous temperature inversion, subsequently suppressing the vertical turbulent diffusion
377 and decreasing the PBLH to further trap more air pollutants and water vapor to increase the
378 RH in the PBL. Increasing RH enhances aerosol hygroscopic growth and multiphase
379 reactions and augments the particle size and mass, causing further dimming and decrease of
380 the TSFC and PBLH. The whole process constitutes a positive feedback induced by the
381 aerosol radiation effect to enhance near-surface [PM_{2.5}], which has been proposed in many
382 studies (Quan et al., 2013; Petaja et al., 2016; Yang et al., 2016; Tie et al., 2017; Ding et al.,
383 2017; Liu et al., 2018). The noted positive meteorological condition feedback has also been
384 considered as the main reason for the near-surface PM_{2.5} explosive growth (Zhong et al., 2018;
385 X. Y. Zhang et al., 2018).

386 To comprehensively evaluate the influence of the ARF on near-surface [PM_{2.5}] during
387 the haze episode, a sensitivity study has been conducted, in which the ARF is turned off
388 (hereafter referred as f_{rad0}). Therefore, the contribution of the ARF to near-surface [PM_{2.5}]
389 can be determined by the difference between f_{base} and f_{rad0} ($f_{base} - f_{rad0}$). The most
390 polluted area in NCP is first selected to verify the conceptual model of the ARF contribution
391 to the heavy haze formation, with the average near-surface [PM_{2.5}] during the haze episode
392 exceeding 150 $\mu\text{g m}^{-3}$. Figure 11 provides the temporal variation of near-surface [PM_{2.5}],
393 SWDOWN, TSFC, PBLH, and RH averaged in the selected area during the episode in f_{base}
394 and f_{rad0} . Apparently, the ARF considerably decreases the solar radiation reaching the
395 ground surface and correspondingly lowers the TSFC (Figures 11b and 11c). Subsequently,



396 the PBLH is decreased and the surface RH is increased due to decreasing TSFC during
397 daytime (Figures 11d and 11e). However, the variation trend of near-surface $[PM_{2.5}]$, PBLH,
398 TSFC and RH due to the ARF is not similar to that proposed in the conceptual model. During
399 the haze development stage, whether the ARF is considered or not, the TSFC and RH exhibit
400 an increasing trend, showing the air mass originated from the south, and the PBLH does not
401 consistently decrease with increasing near-surface $[PM_{2.5}]$. Additionally, the ARF
402 contribution to near-surface $[PM_{2.5}]$ is generally marginal during the haze development stage.
403 During the haze maturation stage, the ARF commences to elevate near-surface $[PM_{2.5}]$
404 appreciably. It is worth noting that, even if the ARF is not considered in f_{rad0} , the heavy
405 haze pollution still occurs during the episode. For example, from 17 to 20 December 2015,
406 without the ARF, near-surface $[PM_{2.5}]$ still continue to increase from around 30 to 300 $\mu\text{g m}^{-3}$,
407 and fluctuates between 150 to 300 $\mu\text{g m}^{-3}$ until the occurrence of favorable meteorological
408 conditions on 25 December. Hence, according to the variation trend of near-surface $[PM_{2.5}]$
409 with and without the ARF contribution, the continuous accumulation of $PM_{2.5}$ during the haze
410 episode is not primarily caused by the ARF, but predominantly induced by the stagnant
411 meteorological conditions as well as the massive air pollutants emissions in NCP.

412 In order to quantitatively evaluate effects of the ARF on near-surface $[PM_{2.5}]$, which
413 cannot be reflected by the temporal variation of near-surface $[PM_{2.5}]$, TSFC, PBLH and RH,
414 an ensemble method is used in this study. The daytime near-surface $[PM_{2.5}]$ in NCP during
415 the episode in f_{base} are first subdivided into 30 bins with an interval of 20 $\mu\text{g m}^{-3}$. The
416 SWDOWN, TSFC, PBLH, the near-surface WSPD, RH, and $[PM_{2.5}]$ in f_{base} and f_{rad0} in
417 the same grid cell are assembled as the bin $[PM_{2.5}]$, respectively, and an average of these
418 variables in each bin are calculated. Figure 12 shows the decrease of SWDOWN (%), TSFC
419 ($^{\circ}\text{C}$), PBLH (%), WSPD (m s^{-2}), and the increase of RH (%), not percentage change) and
420 near-surface $[PM_{2.5}]$ contribution (%) caused by the ARF as a function of bin $[PM_{2.5}]$. The



421 SWDOWN reaching the ground surface almost decreases linearly with the enhancement of
422 near-surface $[PM_{2.5}]$. When the ARF is considered, aerosols in the atmosphere absorb or
423 scatter the incoming solar radiation, directly attenuating the radiation reaching the ground
424 surface. When near-surface $[PM_{2.5}]$ exceed $200 \mu\text{g m}^{-3}$, the SWDOWN at ground surfaces
425 decreases by more than 20% (Figure 12a). Moreover, the decrease of the SWDOWN
426 correspondingly lowers the TSFC and the decrease of the TSFC is generally proportional to
427 near-surface $[PM_{2.5}]$, about $0.35 \text{ }^\circ\text{C}$ per $100 \mu\text{g m}^{-3} PM_{2.5}$ (Figure 12b). Interestingly, the ARF
428 also decreases near-surface WSPD by about $0.1\sim 0.2 \text{ m s}^{-1}$ with near-surface $[PM_{2.5}]$
429 exceeding $80 \mu\text{g m}^{-3}$ (Figure 12c). When severe air pollution occurs in NCP during
430 wintertime, atmospheric convergence occurs in the PBL (Liao et al., 2015; Ding et al., 2017).
431 However, the ARF induced cooling in the low-level air generates a divergence in NCP,
432 causing the decrease of near-surface WSPD.

433 The PBLH is primarily determined by the atmospheric dynamic and thermal condition of
434 ground surfaces. Therefore, the decrease of WSPD and TSFC due to the ARF subsequently
435 suppresses the PBL development and diminishes the PBLH (Figure 12d). When near-surface
436 $[PM_{2.5}]$ are less than $250 \mu\text{g m}^{-3}$, the PBLH decreases rapidly with increasing $[PM_{2.5}]$. When
437 the near-surface $[PM_{2.5}]$ are between $250 \mu\text{g m}^{-3}$ and $350 \mu\text{g m}^{-3}$, the decrease of PBLH is
438 around 28%. With near-surface $[PM_{2.5}]$ more than $350 \mu\text{g m}^{-3}$, the decrease of PBLH exceeds
439 30%. As for the ARF effect on water vapor in the PBL, the conceptual model has proposed
440 that the decreased PBL induced by the ARF weakens the vertical exchange of water vapor or
441 the dispersion of water vapor is constrained by the shallow PBL (Tie et al., 2017; Liu et al.,
442 2018). However, Figure 13a shows that the ARF decrease the near-surface water vapor
443 content slightly, by more than 0.1 g kg^{-1} with near-surface $[PM_{2.5}]$ exceeding $100 \mu\text{g m}^{-3}$.
444 During the haze episode in NCP, the abundant moisture in the PBL is mainly transported
445 from the south. The divergence due to cooling caused by the ARF weakens the prevailing



446 southerly wind and decreases the moisture transport from the south, reducing the water vapor
447 content in NCP. Considering that the RH is sensitive to the temperature with a constant water
448 vapor content, the ARF induced cooling still increases the near-surface RH (Figure 12e).
449 When near-surface $[PM_{2.5}]$ exceed $300 \mu\text{g m}^{-3}$, the RH is increased by more than 5%, so the
450 heavy haze generally causes the air to be more humid.

451 More $PM_{2.5}$ emitted or formed are trapped by a shallow PBL caused by the ARF, and
452 increased RH promotes the aerosol hygroscopic growth and further multiphase reactions,
453 progressively enhancing near-surface $[PM_{2.5}]$ (Figure 12f). When near-surface $[PM_{2.5}]$ are
454 more than $50 \mu\text{g m}^{-3}$, the contribution of the ARF to near-surface $[PM_{2.5}]$ consistently
455 increases with the haze deterioration. When the severe haze occurs, i.e., near-surface $[PM_{2.5}]$
456 exceed $250 \mu\text{g m}^{-3}$, more than 12% or $30 \mu\text{g m}^{-3}$ $PM_{2.5}$ is contributed by the ARF. The
457 simulated ARF effects on near-surface $[PM_{2.5}]$ are generally comparable to those reported by
458 previous studies. Z. Wang et al. (2014) have shown that the ARF increases the monthly $PM_{2.5}$
459 concentration by 10%-30% in Beijing-Tianjin-Hebei in January 2013. Using the
460 WRF-CHEM model, Gao et al. (2015) have indicated that the ARF increases the $PM_{2.5}$
461 concentration by $10\text{-}50 \mu\text{g m}^{-3}$ (2%-30%) over Beijing, Tianjin, and south Hebei from 10 to
462 15 January 2013, a period with the simulated maximum hourly surface $PM_{2.5}$ concentration
463 of more than $600 \mu\text{g m}^{-3}$. X. Zhang et al. (2018) have also quantified the aerosol-meteorology
464 interaction effect on $PM_{2.5}$ concentrations in China in 2014 using the WRF-CHEM model,
465 showing that the increase of $PM_{2.5}$ concentrations associated with the ARF is up to 16% in
466 China. Other previous studies have also confirmed the ARF effect during the heavy haze
467 pollution episode (Wang et al., 2015; Zhang et al., 2015; Gao et al., 2016). However, when
468 near-surface $[PM_{2.5}]$ are less than $50 \mu\text{g m}^{-3}$, the contribution of the ARF to near-surface
469 $[PM_{2.5}]$ is negative, although the ARF decreases PBLH and increases RH. One of the possible
470 reasons for the negative contribution of the ARF is perturbations of wind fields caused by the



471 ARF induced cooling. Figure 13b presents the average vertical velocity below about 400 m in
472 f_{rad0} as a function of near-surface $[PM_{2.5}]$. Apparently, when the ARF is not considered, the
473 area with near-surface $[PM_{2.5}]$ less than $100 \mu\text{g m}^{-3}$ is generally controlled by downward
474 airflow, and vice versa for the area with near-surface $[PM_{2.5}]$ more than $100 \mu\text{g m}^{-3}$. The ARF
475 induced cooling generally cause a downward motion in the PBL (Figure 13c), which
476 suppresses the upward motion in the area with near-surface $[PM_{2.5}]$ more than $100 \mu\text{g m}^{-3}$ to
477 enhance near-surface $[PM_{2.5}]$, but accelerates the downward motion in the area with
478 near-surface $[PM_{2.5}]$ less than $100 \mu\text{g m}^{-3}$ to decrease near-surface $[PM_{2.5}]$. Countered by the
479 decrease of PBLH and increase of RH, the ARF contribution becomes positive with
480 near-surface $[PM_{2.5}]$ exceeding $50 \mu\text{g m}^{-3}$.

481 Figure 14 presents spatial distributions of the average near-surface $PM_{2.5}$ contribution
482 due to the ARF during the episode. The average near-surface $PM_{2.5}$ contribution caused by
483 the ARF in NCP is $10.2 \mu\text{g m}^{-3}$ or 7.8%, with the maximum exceeding $40 \mu\text{g m}^{-3}$ in the south
484 of Hebei. On average, the ARF contribution to near-surface $[PM_{2.5}]$ is the most significant in
485 Tianjin, about $17.6 \mu\text{g m}^{-3}$ or 10.3%, followed by Hebei ($11.6 \mu\text{g m}^{-3}$ or 9.3%), Shandong
486 ($11.5 \mu\text{g m}^{-3}$ or 7.3%), Henan ($11.2 \mu\text{g m}^{-3}$ or 7.7%), Anhui ($7.7 \mu\text{g m}^{-3}$ or 7.4%), Beijing (7.3
487 $\mu\text{g m}^{-3}$ or 6.9%), and Jiangsu ($7.0 \mu\text{g m}^{-3}$ or 6.2%). It is noteworthy that the ARF contribution
488 during the episode in North China is generally positive, but in its surrounding area the
489 contribution becomes negative. At a large scale, when the air pollution occurs during
490 wintertime in North China, the vertical motion over the polluted area generally shows an
491 ascending-descending-ascending distribution from the surface to the middle level of the
492 troposphere, and wind directions present a structure of convergence-divergence-convergence
493 accordingly (Liao et al., 2015; Wu et al., 2017; Ding et al., 2017). The ARF cools the
494 low-level atmosphere and induces a downward motion, which suppresses the upward motion
495 in the convergence area in North China to increase near-surface $[PM_{2.5}]$, but accelerates the



496 downward motion in the divergence area to decrease $[PM_{2.5}]$.

497 Furthermore, when the ARF is considered, near-surface $[PM_{2.5}]$ over the East and South
498 China Sea are also increased, with an enhancement less than $5 \mu\text{g m}^{-3}$ (about 3% to more than
499 15%). Considering the low near-surface $[PM_{2.5}]$ over sea, the $[PM_{2.5}]$ enhancement might be
500 caused by the $PM_{2.5}$ transport from the continent. Figure 15 shows the spatial distribution of
501 the TSFC and wind field variation caused by the ARF averaged during the episode.
502 Apparently, the ARF causes a widespread cooling effect in East China, and the cooling is the
503 most significant in NCP, with the maximum TSFC decrease exceeding 1.5°C . The cooling
504 effect in NCP induces a weak northerly wind, decreasing the prevailing southerly wind
505 during the haze episode (Figure 15). Additionally, the cooling effect over the continent also
506 intensifies the temperature contrast between land and sea, producing a secondary circulation
507 to transport the $PM_{2.5}$ from the continent to the East and South China Sea.

508

509 4 Summary and conclusions

510 In the study, a persistent haze pollution episode in NCP from 05 December 2015 to 04
511 January 2016 are simulated using the WRF-CHEM model to verify the ARF contribution to
512 the haze formation. Generally, the model reproduces well the spatial distributions and
513 temporal variations of $PM_{2.5}$, O_3 , NO_2 , SO_2 , and CO mass concentrations against observations
514 in NCP. The calculated temporal variations of aerosol species are also consistent with the
515 ACSM measurement in Beijing, particularly with regard to the simulation of sulfate, nitrate,
516 and ammonium. Moreover, the model simulates reasonably well the variation of SWDOWN,
517 PBLH, and aerosol radiative properties during the episode, compared to the measurement.

518 Previous studies have established that a positive feedback induced by the ARF causes
519 the heavy haze formation by modulating the PBL and RH. However, model results
520 demonstrate that during the haze development stage in NCP, the ARF does not dominate



521 accumulation of near-surface $[PM_{2.5}]$. The TSFC and RH generally exhibit an increasing
522 trend, showing that the air mass originated from the south, and the PBLH does not
523 consistently decrease as proposed with increasing near-surface $[PM_{2.5}]$. During the haze
524 maturation stage, the ARF considerably enhances near-surface $[PM_{2.5}]$.

525 Ensemble analyses of model results show that, during daytime, the ARF attenuates
526 SWDOWN reaching ground surfaces efficiently with increasing near-surface $[PM_{2.5}]$ in NCP,
527 and SWDOWN is decreased by more than 20% when near-surface $[PM_{2.5}]$ exceed $200 \mu\text{g m}^{-3}$.
528 Correspondingly, the TSFC progressively decreases with increasing near-surface $[PM_{2.5}]$,
529 with a rate of around $0.35 \text{ }^\circ\text{C}$ per $100 \mu\text{g m}^{-3} PM_{2.5}$. The ARF induced cooling generates a
530 divergence in the low-level atmosphere in NCP, lowering the near-surface WSPD and
531 decreasing the water vapor transport from the south. The decreased WSPD and TSFC caused
532 by the ARF hinder the PBL development and the PBLH decreases rapidly with increasing
533 near-surface $[PM_{2.5}]$. When near-surface $[PM_{2.5}]$ exceed $250 \mu\text{g m}^{-3}$, the PBLH is decreased
534 by over 28%. Although the water content in NCP is decreased slightly, the RH is still
535 increased due to the ARF induced cooling, and the RH enhancement exceeds 5% when
536 near-surface $[PM_{2.5}]$ are more than $300 \mu\text{g m}^{-3}$. A shallow PBL and more humid air caused by
537 the ARF accelerate the $PM_{2.5}$ accumulation and secondary pollutant formation, facilitating
538 heavy haze formation. The contribution of the ARF to near-surface $[PM_{2.5}]$ increases from 12%
539 to 20% when near-surface $[PM_{2.5}]$ increase from 250 to $500 \mu\text{g m}^{-3}$. However, the ARF
540 decreases the $PM_{2.5}$ level with near-surface $[PM_{2.5}]$ less than $50 \mu\text{g m}^{-3}$.

541 The average near-surface $PM_{2.5}$ contribution of the ARF during the episode in NCP is
542 $10.2 \mu\text{g m}^{-3}$ or 7.8%. The ARF aggravates the heavy haze formation in North China, but in its
543 surrounding area the ARF slightly mitigates the haze pollution. Generally, there is a structure
544 of convergence-divergence-convergence over the polluted area of North China from the
545 surface to the middle level of the troposphere. The ARF causes a widespread cooling effect in



546 East China, particularly remarkable in NCP. A downward motion is induced due to the
547 cooling of the low-level atmosphere, impeding the upward motion in the convergence area in
548 North China to increase near-surface $[PM_{2.5}]$, but accelerating the downward motion in the
549 divergence area to decrease $[PM_{2.5}]$.

550 Although the model performs generally well in simulating air pollutants, aerosol species
551 and radiative properties, SWDOWN, and PBLH, the uncertainties from meteorological fields
552 and emission inventory still have potentials to influence the ARF evaluation. Particularly,
553 further studies need to be conducted to improve the AOD simulations. In this study, the ARF
554 only considers the aerosol effect on the solar radiation, and the influence of longwave
555 radiation also needs to be included. In addition, aerosols play an important role in the cloud
556 process serving as cloud condensation nuclei (CCN) and ice nuclei (IN). Therefore,
557 aerosol-cloud interactions (aerosol indirect effect) modify temperature and moisture profiles
558 and further influence precipitation, leading to potential effects on the atmospheric chemistry
559 (Wang et al., 2011). Future studies should be performed to investigate the feedbacks of the
560 aerosol indirect effect on the air pollutants.

561

562

563 *Author contribution.* Guohui Li, as the contact author, provided the ideas and financial
564 support, developed the model code, verified the conclusions, and revised the paper. Jiarui Wu
565 conducted a research, designed the experiments, carried the methodology out, performed the
566 simulation, processed the data, prepared the data visualization, and prepared the manuscript
567 with contributions from all authors. Naifang Bei provided the treatment of meteorological
568 data, analyzed the study data, validated the model performance, and reviewed the manuscript.
569 Bo Hu provided the observation data used in the study, synthesized the observation, and
570 reviewed the paper. Suixin Liu, Meng Zhou, Qiyuan Wang, Zirui Liu, and Yichen Wang



571 provided the data and the primary data process, and reviewed the manuscript. Xia Li, Lang
572 Liu, and Tian Feng analyzed the initial simulation data, visualized the model results and
573 reviewed the paper. Junji Cao, Xuexi Tie, Jun Wang provided critical reviews pre-publication
574 stage. Luisa T. Molina provided a critical preview and financial support, and revised the
575 manuscript.

576

577

578 *Acknowledgements.* This work is financially supported by the National Key R&D Plan
579 (Quantitative Relationship and Regulation Principle between Regional Oxidation Capacity of
580 Atmospheric and Air Quality (2017YFC0210000)) and National Research Program for Key
581 Issues in Air Pollution Control. Luisa Molina acknowledges support from US NSF Award
582 1560494.

583

584

585

586

587

**588 Reference**

- 589** Ackerman, T. P.: Model of effect of aerosols on urban climates with particular applications to
590 Los-Angeles basin, *J. Atmos. Sci.*, 34, 531-547,
591 10.1175/1520-0469(1977)034<0531:amoteo>2.0.co;2, 1977.
- 592** Bei, N., Lei, W., Zavala, M., and Molina, L. T.: Ozone predictabilities due to meteorological
593 uncertainties in the Mexico City basin using ensemble forecasts, *Atmos. Chem. Phys.*, 10,
594 6295-6309, 10.5194/acp-10-6295-2010, 2010.
- 595** Bei, N., Li, G., and Molina, L. T.: Uncertainties in SOA simulations due to meteorological
596 uncertainties in Mexico City during MILAGRO-2006 field campaign, *Atmos. Chem.*
597 *Phys.*, 12, 11295-11308, 10.5194/acp-12-11295-2012, 2012.
- 598** Bei, N., Wu, J., Elser, M., Feng, T., Cao, J., El-Haddad, I., Li, X., Huang, R., Li, Z., Long, X.,
599 Xing, L., Zhao, S., Tie, X., Prévôt, A. S. H., and Li, G.: Impacts of meteorological
600 uncertainties on the haze formation in Beijing-Tianjin-Hebei (BTH) during wintertime: a
601 case study, *Atmos. Chem. Phys.*, 17, 14579-14591,
602 <https://doi.org/10.5194/acp-17-14579-2017>, 2017.
- 603** Binkowski, F. S. and Roselle S. J.: Models-3 Community Multiscale Air Quality (CMAQ)
604 model aerosol component: 1. Model description, *J. Geophys. Res.*, 108, 4183,
605 doi:10.1029/2001JD001409, 2003.
- 606** Boucher, O., Randall, D., Artaxo, P., Bretherton, C., Feingold, G., Forster, P., Kerminen, V.
607 M., Kondo, Y., Liao, H., Lohmann, U., Rasch, P., Satheesh, S. K., Sherwood, S., Stevens,
608 B., and Zhang, X. Y. : Clouds and aerosols. In: *Climate Change 2013: The Physical*
609 *Science Basis. Contribution of Working Group I to the Fifth Assessment Report of the*
610 *Intergovernmental Panel on Climate Change. Cambridge University Press, Cambridge,*
611 *United Kingdom and New York, NY, USA, 2013.*
- 612** Chand, D., Wood, R., Ghan, S. J., Wang, M. H., Ovchinnikov, M., Rasch, P. J., Miller, S.,
613 Schichtel, B., and Moore, T.: Aerosol optical depth increase in partly cloudy conditions, *J.*
614 *Geophys. Res.-Atmos.*, 117, 8, 10.1029/2012jd017894, 2012.
- 615** Cheng, Y. F., Zheng, G. J., Wei, C., Mu, Q., Zheng, B., Wang, Z. B., Gao, M., Zhang, Q., He,
616 K. B., Carmichael, G., Poschl, U., and Su, H.: Reactive nitrogen chemistry in aerosol
617 water as a source of sulfate during haze events in China, *Sci. Adv.*, 2, 11,
618 10.1126/sciadv.1601530, 2016.
- 619** China MEP (Ministry of Environmental Protection, China): Air Quality Observation
620 Real-time Release Platform of MEP Data Center, available at:
621 <http://106.37.208.233:20035/> (last access: 18 October 2018), 2013a.
- 622** China MEP (Ministry of Environmental Protection, China): Online Monitoring and Analysis
623 Platform of China Air Quality, available at: <http://www.aqistudy.cn/> (last access: 18
624 October 2018), 2013b.
- 625** Chen, F. and Dudhia, J.: Coupling an advanced land surface-hydrology model with the Penn
626 State-NCAR MM5 modeling system. Part I: Model implementation and sensitivity, *Mon.*



- 627 Weather Rev., 129(4), 569-585, 2001.
- 628 Chou, M.-D. and Suarez, M. J.: A solar radiation parameterization for atmospheric studies,
629 NASA Tech. Rep. NASA/TM-1999- 10460, 15, 38 pp., 1999.
- 630 Chou, M.-D. and Suarez, M. J.: A thermal infrared radiation parameterization for
631 atmospheric studies, NASA/TM-2001-104606, 19, 55 pp., 2001.
- 632 d'Almeida, Koepke, G. A., P., and Shettle, E. P.: Atmospheric aerosols: global climatology
633 and radiative Characteristics, 261 pp., A. Deepak, Hampton, Va., 1991.
- 634 Ding, A. J., Fu, C. B., Yang, X. Q., Sun, J. N., Petaja, T., Kerminen, V. M., Wang, T., Xie,
635 Y., Herrmann, E., Zheng, L. F., Nie, W., Liu, Q., Wei, X. L., and Kulmala, M.: Intense
636 atmospheric pollution modifies weather: a case of mixed biomass burning with fossil fuel
637 combustion pollution in eastern China, Atmos. Chem. Phys., 13, 10545-10554,
638 10.5194/acp-13-10545-2013, 2013.
- 639 Ding, A. J., Huang, X., Nie, W., Sun, J. N., Kerminen, V. M., Petäjä, T., Su, H., Cheng, Y. F.,
640 Yang, X. Q., and Wang, M. H.: Enhanced haze pollution by black carbon in megacities in
641 China, Geophys. Res. Lett., 43, doi:10.1002/2016GL067745, 2016.
- 642 Ding, Y. H., Wu, P., Liu, Y. J., and Song, Y. F.: Environmental and Dynamic Conditions for
643 the Occurrence of Persistent Haze Events in North China, Engineering., 3, 266-271,
644 10.1016/j.eng.2017.01.009, 2017.
- 645 Engstrom, A., and Ekman, A. M. L.: Impact of meteorological factors on the correlation
646 between aerosol optical depth and cloud fraction, Geophys. Res. Lett., 37, 4,
647 10.1029/2010gl044361, 2010.
- 648 Fast, J. D., Gustafson, W. I., Easter, R. C., Zaveri, R. A., Barnard, J. C., Chapman, E. G.,
649 Grell, G., and Peckham, S. E.: Evolution of Ozone, Particulates, and Aerosol Direct
650 Radiative Forcing in the Vicinity of Houston Using a Fully Coupled
651 Meteorology-Chemistry-Aerosol Model, J. Geophys. Res.-Atmos., 11, D21,
652 111(D21):D21305, Medium: X, 2006.
- 653 Fu, J. S., Hsu, N. C., Gao, Y., Huang, K., Li, C., Lin, N. H., and Tsay, S. C.: Evaluating the
654 influences of biomass burning during 2006 BASE-ASIA: a regional chemical transport
655 modeling, Atmos. Chem. Phys., 12, 3837-3855, 10.5194/acp-12-3837-2012, 2012.
- 656 Gao, M., Carmichael, G. R., Wang, Y., Saide, P. E., Yu, M., Xin, J., Liu, Z., and Wang, Z.:
657 Modeling study of the 2010 regional haze event in the North China Plain, Atmos. Chem.
658 Phys., 16, 1673-1691, 10.5194/acp-16-1673-2016, 2016.
- 659 Gao, Y., Zhang, M., Liu, Z., Wang, L., Wang, P., Xia, X., and Tao, M.: Modeling the
660 feedback between aerosol and meteorological variables in the atmospheric boundary layer
661 during a severe fog-haze event over the North China Plain, Atmos. Chem. Phys., 15,
662 1093-1130, 2015.
- 663 Guo, S., Hu, M., Zamora, M. L., Peng, J. F., Shang, D. J., Zheng, J., Du, Z. F., Wu, Z., Shao,
664 M., Zeng, L. M., Molina, M. J., and Zhang, R. Y.: Elucidating severe urban haze
665 formation in China, P. Natl. Acad. Sci. USA., 111, 17373-17378,



- 666 10.1073/pnas.1419604111, 2014.
- 667 Grandey, B. S., Stier, P., and Wagner, T. M.: Investigating relationships between aerosol
668 optical depth and cloud fraction using satellite, aerosol reanalysis and general circulation
669 model data, *Atmos. Chem. Phys.*, 13, 3177-3184, [10.5194/acp-13-3177-2013](https://doi.org/10.5194/acp-13-3177-2013), 2013.
- 670 Grell, G. A. and Devenyi, D.: A generalized approach to parameterizing convection
671 combining ensemble and data assimilation techniques, *Geophys. Res. Lett.*, 29(14),
672 doi:10.1029/2002GL015311, 2002.
- 673 Grell, G. A., Peckham, S. E., Schmitz, R., McKeen, S. A., Frost, G., Skamarock, W. C., and
674 Eder, B.: Fully coupled “online” chemistry within the WRF model, *Atmos. Environ.*, 39,
675 6957-6975, [10.1016/j.atmosenv.2005.04.027](https://doi.org/10.1016/j.atmosenv.2005.04.027), 2005.
- 676 Grell, G., Freitas, S. R., Stuefer, M., and Fast, J.: Inclusion of biomass burning in
677 WRF-Chem: impact of wildfires on weather forecasts, *Atmos. Chem. Phys.*, 11,
678 5289-5303, [10.5194/acp-11-5289-2011](https://doi.org/10.5194/acp-11-5289-2011), 2011.
- 679 Guenther, A., Karl, T., Harley, P., Wiedinmyer, C., Palmer, P. I., and Geron, C.: Estimates of
680 global terrestrial isoprene emissions using MEGAN (Model of Emissions of Gases and
681 Aerosols from Nature), *Atmos. Chem. Phys.*, 6, 3181-3210,
682 <https://doi.org/10.5194/acp-6-3181-2006>, 2006.
- 683 Hong, S.-Y. and Lim, J.-O. J.: The WRF Single-Moment 6-Class Microphysics Scheme
684 (WSM6), *Asia-Pacific J. Atmos. Sci.*, 42, 129-151, 2006.
- 685 Horowitz, L. W., Walters, S., Mauzerall, D. L., Emmons, L. K., Rasch, P. J., Granier, C., Tie,
686 X. X., Lamarque, J. F., Schultz, M. G., Tyndall, G. S., Orlando, J. J., and Brasseur, G. P.:
687 A global simulation of tropospheric ozone and related tracers: Description and evaluation
688 of MOZART, version 2, *J. Geophys. Res.-Atmos.*, 108, 4784,
689 <https://doi.org/10.1029/2002jd002853>, 2003.
- 690 Intergovernmental Panel on Climate Change (IPCC). The Physical Science Basis of Climate
691 Change: Changes in Atmospheric Constituents and in Radiative Forcing. Cambridge
692 University Press, New York, pp. 26-27, 2007.
- 693 Jacobson, M. Z.: Studying the effects of aerosols on vertical photolysis rate coefficient and
694 temperature profiles over an urban airshed, *J. Geophys. Res.-Atmos.*, 103, 10593-10604,
695 [10.1029/98jd00287](https://doi.org/10.1029/98jd00287), 1998.
- 696 Jacobson, M. Z.: Analysis of aerosol interactions with numerical techniques for solving
697 coagulation, nucleation, condensation, dissolution, and reversible chemistry among
698 multiple size distributions, *J. Geophys. Res.-Atmos.*, 107, 23, [10.1029/2001jd002044](https://doi.org/10.1029/2001jd002044),
699 2002.
- 700 Janjić, Z. I.: Nonsingular Implementation of the Mellor -Yamada Level 2.5 Scheme in the
701 NCEP Meso Model, Ncep Office Note, 436, 2002.
- 702 Kawamoto, K., Hayasaka, T., Uno, I., and Ohara, T.: A cor- relative study on the relationship
703 between modeled anthro- pogenic aerosol concentration and satellite-observed cloud
704 properties over east Asia, *J. Geophys. Res.-Atmos.*, 111, 7, doi:10.1029/2005jd006919,



- 705 2006.
- 706 Koch, D., and Del Genio, A. D.: Black carbon semi-direct effects on cloud cover: review and
707 synthesis, *Atmos. Chem. Phys.*, 10, 7685-7696,
708 <http://dx.doi.org/10.5194/acp-10-7685-2010>, 2010.
- 709 Liao, X., Sun, Z., Tang, Y., Pu, W., Li, Z., and Lu, B.: Meteorological mechanism for the
710 formation of a serious pollution case in Beijing in the background of northerly flow at
711 upper levels, *Environmental Science*, 36, 801-808, 2015. (in Chinese)
- 712 Li, G., Zhang, R., Fan, J., and Tie, X.: Impacts of black carbon aerosol on photolysis and
713 ozone, *J. Geophys. Res.*, 110, 10.1029/2005jd005898, 2005.
- 714 Li, G., Wang, Y., and Zhang, R.: Implementation of a two-moment bulk microphysics scheme
715 to the WRF model to investigate aerosol-cloud interaction, *J. Geophys. Res.*, 113,
716 D15211, doi:10.1029/2007JD009361, 2008a.
- 717 Li, G., Wang, Y., Lee, K.-H., Diao, Y., and Zhang, R.: Increased winter precipitation over the
718 North Pacific from 1984-1994 to 1995-2005 inferred from the Global Precipitation
719 Climatology Project, *Geophys. Res. Lett.*, 35, L13821, doi:10.1029/2008GL034668,
720 2008b.
- 721 Li, G., Wang, Y., Lee, K.-H., Diao, Y., and Zhang, R.: Impacts of aerosols on the
722 development and precipitation of a mesoscale squall line, *J. Geophys. Res.*,
723 doi:10.1029/2008JD011581, 2009.
- 724 Li, G., Lei, W., Zavala, M., Volkamer, R., Dusanter, S., Stevens, P., and Molina, L. T.:
725 Impacts of HONO sources on the photochemistry in Mexico City during the
726 MCMA-2006/MILAGO Campaign, *Atmos. Chem. Phys.*, 10, 6551-6567,
727 10.5194/acp-10-6551-2010, 2010.
- 728 Li, G., Bei, N., Tie, X., and Molina, L. T.: Aerosol effects on the photochemistry in Mexico
729 City during MCMA-2006/MILAGRO campaign, *Atmos. Chem. Phys.*, 11, 5169-5182,
730 10.5194/acp-11-5169-2011, 2011a.
- 731 Li, G., Zavala, M., Lei, W., Tsimpidi, A. P., Karydis, V. A., Pandis, S. N., Canagaratna, M. R.,
732 and Molina, L. T.: Simulations of organic aerosol concentrations in Mexico City using
733 the WRF-CHEM model during the MCMA-2006/MILAGRO campaign, *Atmos. Chem.*
734 *Phys.*, 11, 3789-3809, 10.5194/acp-11-3789-2011, 2011b.
- 735 Li, G., Lei, W., Bei, N., and Molina, L. T.: Contribution of garbage burning to chloride and
736 PM_{2.5} in Mexico City, *Atmos. Chem. Phys.*, 12, 8751-8761, 10.5194/acp-12-8751-2012,
737 2012.
- 738 Li, G., Bei, N., Cao, J., Huang, R., Wu, J., Feng, T., Wang, Y., Liu, S., Zhang, Q., Tie, X., and
739 Molina, L. T.: A possible pathway for rapid growth of sulfate during haze days in China,
740 *Atmos. Chem. Phys.*, 17, 3301-3316, <https://doi.org/10.5194/acp-17-3301-2017>, 2017a.
- 741 Li, G., Bei, N., Cao, J., Wu, J., Long, X., Feng, T., Dai, W., Liu, S., Zhang, Q., and Tie, X.:
742 Widespread and persistent ozone pollution in eastern China during the non-winter
743 season of 2015: observations and source attributions, *Atmos. Chem. Phys.*, 17,
744 2759-2774, <https://doi.org/10.5194/acp-17-2759-2017>, 2017b.
- 745 Li, X., Wu, J. R., Elser, M., Feng, T., Cao, J. J., El-Haddad, I., Huang, R. J., Tie, X. X.,



- 746 Prevot, A. S. H., and Li, G. H.: Contributions of residential coal combustion to the air
747 quality in Beijing-Tianjin-Hebei (BTH), China: a case study, *Atmos. Chem. Phys.*, 18,
748 10675-10691, 10.5194/acp-18-10675-2018, 2018.
- 749 Liu, Q., Jia, X. C., Quan, J. N., Li, J. Y., Li, X., Wu, Y. X., Chen, D., Wang, Z. F., and Liu, Y.
750 G.: New positive feedback mechanism between boundary layer meteorology and
751 secondary aerosol formation during severe haze events, *Sci. Rep.*, 8, 8,
752 10.1038/s41598-018-24366-3, 2018.
- 753 Nakajima, T., Higurashi, A., Kawamoto, K., and Penner, J. E.: A possible correlation between
754 satellite-derived cloud and aerosol microphysical parameters, *Geophys. Res. Lett.*, 28,
755 1171-1174, doi:10.1029/2000gl012186, 2001.
- 756 Nenes, A., Pandis, S. N., and Pilinis, C.: ISORROPIA: A new thermodynamic equilibrium
757 model for multiphase multicomponent inorganic aerosols, *Aquat. Geochem.*, 4, 123-152,
758 doi:10.1023/a:1009604003981, 1998.
- 759 Penner, J. E., Xu, L., Liou, C., Assamoi, E., Flanner, M. G., Edwards, R., and McConnell,
760 J.: Atmospheric absorption: Can observations constrain the direct and indirect effect of
761 organic and BC aerosols on climate, American Geophysical Union, AGU Fall Meeting
762 Abstract, 2010.
- 763 Perez, C., Nickovic, S., Pejanovic, G., Baldasano, J. M., and Ozsoy, E.: Interactive
764 dust-radiation modeling: A step to improve weather forecasts, *J. Geophys. Res.-Atmos.*,
765 111, 17, 10.1029/2005jd006717, 2006.
- 766 Petäjä, T., Järvi, L., Kerminen, V. M., Ding, A. J., Sun, J. N., Nie, W., Kujansuu, J., Virkkula,
767 A., Yang, X., and Fu, C. B.: Enhanced air pollution via aerosol-boundary layer feedback
768 in China, *Sci. Rep.*, 6, 18998, 2016.
- 769 Pui, D. Y. H., Chen, S. C., and Zuo, Z. L.: PM_{2.5} in China: Measurements, sources, visibility
770 and health effects, and mitigation, *Particuology.*, 13, 1-26, 10.1016/j.partic.2013.11.001,
771 2014.
- 772 Quan, J., Gao, Y., Zhang, Q., Tie, X., Cao, J., Han, S., Meng, J., Chen, P., and Zhao, D.:
773 Evolution of planetary boundary layer under different weather conditions, and its impact
774 on aerosol concentrations, *Particuology.*, 11, 34-40,
775 <https://doi.org/10.1016/j.partic.2012.04.005>, 2013.
- 776 Santese, M., Perrone, M. R., Zakey, A. S., and Tomasi, F. D.: Modeling of Saharan dust
777 outbreaks over the Mediterranean by RegCM3: case studies, *Atmos. Chem. Phys.*, 10,
778 133-156, <https://doi.org/10.5194/acp-10-133-2010>, 2010.
- 779 Satheesh, S. K., Vinoj, V., and Krishnamoorthy, K.: Assessment of Aerosol Radiative Impact
780 over Oceanic Regions Adjacent to Indian Subcontinent Using Multisatellite Analysis,
781 *Adv. Meteorol.*, 13, 10.1155/2010/139186, 2010.
- 782 Sivaraman, C., McFarlane, S., Chapman E.: Planetary boundary layer (PBL) height value
783 added product (VAP): Radiosonde retrievals [J/OL], U.S. DOE, Office of Science,
784 Office of Biological and Environment Research, DOE/SC-ARM/TR-132, 2013.
785 <http://http://www.doc88.com/p-9032320085477.html> (last access: 25 October 2018).
- 786 Taylor, K: Summarizing multiple aspects of model performance in single diagram, *J.*
787 *Geophys. Res.*, 106, 7183-7192, 2001.



- 788 Tie, X., Huang, R. J., Cao, J., Zhang, Q., Cheng, Y., Su, H., Chang, D., Pöschl, U., Hoffmann,
789 T., and Dusek, U.: Severe Pollution in China Amplified by Atmospheric Moisture, *Sci.*
790 *Rep.*, 7, 15760, 2017.
- 791 Vogel, B., Vogel, H., Bäumer, D., Bangert, M., Lundgren, K., Rinke, R., and Stanelle, T.: The
792 comprehensive model system COSMO-ART-Radiative impact of aerosol on the state of
793 the atmosphere on the regional scale, *Atmos. Chem. Phys.*, 9, 8661-8680,
794 <https://doi.org/10.5194/acp-9-8661-2009>, 2009.
- 795 Wang, G., Zhang, R., Gomez, M. E., Yang, L., Zamora, M. L., Hu, M., Lin, Y., Peng, J., Guo,
796 S., and Meng, J.: Persistent sulfate formation from London Fog to Chinese haze, *P. Natl.*
797 *Acad. Sci. USA.*, 113, 13630, 2016.
- 798 Wang, H., Shi, G. Y., Zhang, X. Y., Gong, S. L., Tan, S. C., Chen, B., Che, H. Z., and Li, T.:
799 Mesoscale modelling study of the interactions between aerosols and PBL meteorology
800 during a haze episode in China Jing-Jin-Ji and its near surrounding region - Part 2:
801 Aerosols' radiative feedback effects, *Atmos. Chem. Phys.*, 15, 3277-3287,
802 [10.5194/acp-15-3277-2015](https://doi.org/10.5194/acp-15-3277-2015), 2015.
- 803 Wang, J., Wang, S., Jiang, J., Ding, A., Zheng, M., Zhao, B., Wong, D. C., Zhou, W., Zheng,
804 G., and Wang, L.: Impact of aerosol-meteorology interactions on fine particle pollution
805 during China's severe haze episode in January 2013, *Environ. Res. Lett.*, 9, 094002,
806 2014.
- 807 Wang, Y., Wan, Q., Meng, W., Liao, F., Tan, H., and Zhang, R.: Long-term impacts of
808 aerosols on precipitation and lightning over the Pearl River Delta megacity area in China,
809 *Atmos. Chem. Phys.*, 11, 12421-12436, <https://doi.org/10.5194/acp-11-12421-2011>,
810 2011.
- 811 Wang, Z. F., Li, J., Wang, Z., Yang, W. Y., Tang, X., Ge, B. Z., Yan, P. Z., Zhu, L. L., Chen, X.
812 S., Chen, H. S., Wand, W., Li, J. J., Liu, B., Wang, X. Y., Wand, W., Zhao, Y. L., Lu, N.,
813 and Su, D. B.: Modeling study of regional severe hazes over mid-eastern China in
814 January 2013 and its implications on pollution prevention and control, *Sci. China-Earth*
815 *Sci.*, 57, 3-13, [10.1007/s11430-013-4793-0](https://doi.org/10.1007/s11430-013-4793-0), 2014.
- 816 Wesely, M. L.: Parameterization of surface resistances to gaseous dry deposition in
817 regional-scale numerical models, *Atmos. Environ.*, 23, 1293-1304,
818 [10.1016/0004-6981\(89\)90153-4](https://doi.org/10.1016/0004-6981(89)90153-4), 1989.
- 819 Wong, D. C., Pleim, J., Mathur, R., Binkowski, F., Otte, T., Gilliam, R., Pouliot, G., Xiu, A.,
820 Young, J. O., and Kang, D.: WRF-CMAQ two-way coupled system with aerosol
821 feedback: software development and preliminary results, *Geosci. Model. Dev.*, 5,
822 299-312, [10.5194/gmd-5-299-2012](https://doi.org/10.5194/gmd-5-299-2012), 2012.
- 823 Wu, P., Ding, Y. H., and Liu, Y. J.: Atmospheric circulation and dynamic mechanism for
824 persistent haze events in the Beijing-Tianjin-Hebei region, *Adv. Atmos. Sci.*, 34,
825 429-440, [10.1007/s00376-016-6158-z](https://doi.org/10.1007/s00376-016-6158-z), 2017.
- 826 Yang, X., Zhao, C., Guo, J., and Wang, Y.: Intensification of aerosol pollution associated with
827 its feedback with surface solar radiation and winds in Beijing, *J. Geophys. Res.-Atmos.*,
828 121, 4093-4099, 2016.
- 829 Zhang, B., Wang, Y., and Hao, J.: Simulating aerosol-radiation-cloud feedbacks on
830 meteorology and air quality over eastern China under severe haze conditions in winter,
831 *Atmos. Chem. Phys.*, 15, 2387-2404, [10.5194/acp-15-2387-2015](https://doi.org/10.5194/acp-15-2387-2015), 2015.



- 832 Zhang, D. F., Zakey, A. S., Gao, X. J., Giorgi, F., and Solmon, F.: Simulation of dust aerosol
833 and its regional feedbacks over East Asia using a regional climate model, *Atmos. Chem.*
834 *Phys.*, 9, 1095-1110, [10.5194/acp-9-1095-2009](https://doi.org/10.5194/acp-9-1095-2009), 2009.
- 835 Zhang, Q., Streets, D. G., Carmichael, G. R., He, K. B., Huo, H., Kannari, A., Klimont, Z.,
836 Park, I. S., Reddy, S., Fu, J. S., Chen, D., Duan, L., Lei, Y., Wang, L. T., and Yao, Z. L.:
837 Asian emissions in 2006 for the NASA INTEX-B mission, *Atmos. Chem. Phys.*, 9,
838 5131-5153, <https://doi.org/10.5194/acp-9-5131-2009>, 2009.
- 839 Zhang, R. Y., Li, G. H., Fan, J. W., Wu, D. L., and Molina, M. J.: Intensification of Pacific
840 storm track linked to Asian pollution, *P. Natl. Acad. Sci. USA.*, 104, 5295-5299,
841 [10.1073/pnas.0700618104](https://doi.org/10.1073/pnas.0700618104), 2007.
- 842 Zhang, R., Suh, I., Zhao, J., Zhang, D., Fortner, E. C., Tie, X., Molina, L. T., and Molina, M.
843 J.: Atmospheric new particle formation enhanced by organic acids, *Science*, 304,
844 1487-1490, 2004.
- 845 Zhang, R., Jing, J., Tao, J., Hsu, S.-C., Wang, G., Cao, J., Lee, C. S. L., Zhu, L., Chen, Z.,
846 Zhao, Y., and Shen, Z.: Chemical characterization and source apportionment of PM_{2.5} in
847 Beijing: seasonal perspective, *Atmos. Chem. Phys.*, 13, 7053-7074,
848 <https://doi.org/10.5194/acp-13-7053-2013>, 2013.
- 849 Zhang, X., Zhang, Q., Hong, C. P., Zheng, Y. X., Geng, G. N., Tong, D., Zhang, Y. X., and
850 Zhang, X. Y.: Enhancement of PM_{2.5} Concentrations by Aerosol-Meteorology
851 Interactions Over China, *J. Geophys. Res.-Atmos.*, 123, 1179-1194,
852 [10.1002/2017jd027524](https://doi.org/10.1002/2017jd027524), 2018a.
- 853 Zhang, X. Y., Zhong, J. T., Wang, J. Z., Wang, Y. Q., and Liu, Y. J.: The interdecadal
854 worsening of weather conditions affecting aerosol pollution in the Beijing area in
855 relation to climate warming, *Atmos. Chem. Phys.*, 18, 5991-5999,
856 [10.5194/acp-18-5991-2018](https://doi.org/10.5194/acp-18-5991-2018), 2018b.
- 857 Zhang, Y., Wen, X. Y., and Jang, C. J.: Simulating chemistry-aerosol-cloud-radiation-climate
858 feedbacks over the continental U.S. using the online-coupled weather research
859 forecasting model with chemistry (WRF/Chem), *Atmos. Environ.*, 44(29), 3568-3582,
860 2010.
- 861 Zhao, J., Levitt, N. P., and Zhang, R.: Heterogeneous chemistry of octanal and 2,
862 4-hexadienal with sulfuric acid, *Geophys. Res. Lett.*, 32, L09802,
863 [doi:10.1029/2004GL022200](https://doi.org/10.1029/2004GL022200), 2005.
- 864 Zhong, J. T., Zhang, X. Y., Dong, Y. S., Wang, Y. Q., Liu, C., Wang, J. Z., Zhang, Y. M., and
865 Che, H. C.: Feedback effects of boundary-layer meteorological factors on cumulative
866 explosive growth of PM_{2.5} during winter heavy pollution episodes in Beijing from 2013
867 to 2016, *Atmos. Chem. Phys.*, 18, 247-258, [10.5194/acp-18-247-2018](https://doi.org/10.5194/acp-18-247-2018), 2018.
868
869
870
871
872


 873 Table 1 Impact of the ARF on near-surface [PM_{2.5}] in China
 874

Reference	Time	Location	Impact on [PM _{2.5}]
Z. Wang et al. (2014)	January 2013	Beijing-Tianjin-Hebei	+10~30%
J. Wang et al. (2014)	January 2013	North China Plain	Up to +140 µg m ⁻³
Gao et al. (2015)	10-15 January 2013	Beijing, Tianjin, and south Hebei	+10-50 µg m ⁻³ (2-30%)
Wang et al. (2015)	7-11 July 2008	Beijing, Tianjin, Hebei, East Shanxi, West Shandong, and North Henan	+14%
Zhang et al. (2015)	January 2013	Henan, Hubei, Guangxi, and Sichuan	Maximum +69.3 µg m ⁻³
Ding et al. (2016)	December 2013	Eastern China and the Sichuan Basin	Up to +100 µg m ⁻³
Gao et al. (2016)	January 2010	Shijiazhuang	More than +20 µg m ⁻³
X. Y. Zhang et al. (2018)	December 2016	Beijing	around +84% of [PM _{2.5}] during cumulative explosive growth
Liu et al. (2018)	15-21 December 2016	North China Plain	+56 µg m ⁻³
X. Zhang et al. (2018)	2014	China	over +16% for the daily maximum [PM _{2.5}]
Zhong et al. (2018)	January 2013, February 2014, December 2015, and December 2016 to 10 January 2017	Beijing	Over +70% of [PM _{2.5}] during cumulative explosive growth

875

876

877

878

879



880 Table 2 WRF-CHEM model configurations.

881

Region	East Asia
Simulation period	05 December 2015 to 04 January 2016
Domain size	400 × 400
Domain center	35°N, 114°E
Horizontal resolution	12 km × 12 km
Vertical resolution	35 vertical levels with a stretched vertical grid with spacing ranging from 30 m near the surface, to 500 m at 2.5 km and 1 km above 14 km
Microphysics scheme	WSM 6-class graupel scheme (Hong and Lim, 2006)
Cumulus scheme	Grell-Devenyi ensemble scheme (Grell and Devenyi, 2002)
Boundary layer scheme	MYJ TKE scheme (Janjić, 2002)
Surface layer scheme	MYJ surface scheme (Janjić, 2002)
Land-surface scheme	Unified Noah land-surface model (Chen and Dudhia, 2001)
Longwave radiation scheme	Goddard longwave scheme (Chou and Suarez, 2001)
Shortwave radiation scheme	Goddard shortwave scheme (Chou and Suarez, 1999)
Meteorological boundary and initial conditions	NCEP 1°×1° reanalysis data
Chemical initial and boundary conditions	MOZART 6-hour output (Horowitz et al., 2003)
Anthropogenic emission inventory	Developed by Zhang et al. (2009) and Li et al. (2017), 2012 base year, and SAPRC-99 chemical mechanism
Biogenic emission inventory	Online MEGAN model developed by Guenther et al. (2006)

882

883

884

885

886



887

Figure Captions

888 Figure 1 (a) WRF-CHEM simulation domain with topography and (b) Beijing-Tianjin-Hebei
889 area. In (a), the blue circles represent centers of cities with ambient monitoring sites
890 in, and the size of blue circles denotes the number of ambient monitoring sites of
891 cities. In (b), the blue and red filled circles denote the NCNST and IRSDE site,
892 respectively, the red filled rectangle denotes the meteorological site. The red numbers
893 denote the CERN sites with the solar radiation measurement. 1: Beijing urban; 2:
894 Jiaozhouwan; 3: Yucheng; 4: Luancheng.

895 Figure 2 Pattern comparisons of simulated (color counters) vs. observed (colored circles)
896 near-surface mass concentrations of (a) $\text{PM}_{2.5}$, (b) O_3 , (c) NO_2 , and (d) SO_2 averaged
897 from 05 December 2015 to 04 January 2016. The black arrows indicate simulated
898 surface winds.

899 Figure 3 Comparison of observed (black dots) and simulated (solid red lines) diurnal profiles
900 of near-surface hourly mass concentrations of (a) $\text{PM}_{2.5}$, (b) O_3 , (c) NO_2 , (d) SO_2 , and
901 (d) CO averaged at monitoring sites in NCP from 05 December 2015 to 04 January
902 2016.

903 Figure 4 Comparison of measured (black dots) and simulated (black line) diurnal profiles of
904 submicron aerosol species of (a) POA, (b) SOA, (c) sulfate, (d) nitrate, and (e)
905 ammonium at NCNST site in Beijing from 05 December 2015 to 04 January 2016.

906 Figure 5 (a) Scatter plot of the MODIS retrieved and simulated daily AOD, (b) Taylor
907 diagram (Taylor, 2001) to present the variance, bias and correlation of the retrieved
908 and simulated daily AOD averaged in NCP from 05 December 2015 to 04 January
909 2016.

910 Figure 6 Spatial distribution of (a) retrieved and (b) simulated AOD averaged from 05
911 December 2015 to 04 January 2016 in NCP.

912 Figure 7 Comparison of measured (black dots) and predicted (red line) diurnal profiles of
913 SSA in Beijing from 05 December 2015 to 04 January 2016.

914 Figure 8 Comparison of measured (black dots) and predicted (red line) diurnal profiles of the
915 SWDOWN reaching the ground surface in (a) Beijing, (b) Jiaozhouwan, (c)
916 Luancheng, and (d) Yucheng from 05 December 2015 to 04 January 2016.

917 Figure 9 Comparison of predicted diurnal profile (red line) of PBLH from 05 December 2015
918 to 04 January 2016 with observations at 12:00 BJT in Beijing.

919 Figure 10 Scatter plot of the PBLH and near-surface $[\text{PM}_{2.5}]$ at IRSDE site from 12 January
920 to 20 February 2014. The black rectangle shows the bin average of PBLH. The color
921 of the filled circles denotes the WSPD at the meteorological site close to IRSDE in
922 Figure 1b.

923 Figure 11 Temporal variations of the average (a) near-surface $[\text{PM}_{2.5}]$, (b) SWDOWN at the
924 ground surface, (c) TSFC, (d) PBLH, and (e) RH in the most polluted area in NCP
925 with $[\text{PM}_{2.5}]$ of more than $150 \mu\text{g m}^{-3}$ in f_{base} (red solid line) and f_{rad0} (blue solid
926 line) from 05 December 2015 to 04 January 2016.

927 Figure 12 Average (a) percentage decrease of SWDOWN at the ground surface, (b) decrease
928 of TSFC, (c) decrease of WSPD, (d) percentage decrease of PBLH, (e) increase of RH,
929 and (f) percentage contribution of near-surface $[\text{PM}_{2.5}]$ caused by the ARF, as a



930 function of the near-surface $[PM_{2.5}]$ in NCP during daytime from 05 December 2015
931 to 04 January 2016.

932 Figure 13 Average (a) decrease of water vapor content and (c) increase of average vertical
933 velocity below 400 m caused by the ARF, and (b) average vertical velocity below 400
934 m as a function of the near-surface $[PM_{2.5}]$ in NCP during daytime from 05 December
935 2015 to 04 January 2016.

936 Figure 14 Near-surface $[PM_{2.5}]$ contribution caused by the ARF, averaged from 05 December
937 2015 to 04 January 2016 in NCP.

938 Figure 15 TSFC and wind filed variations caused by the ARF, averaged from 05 December
939 2015 to 04 January 2016 in NCP.

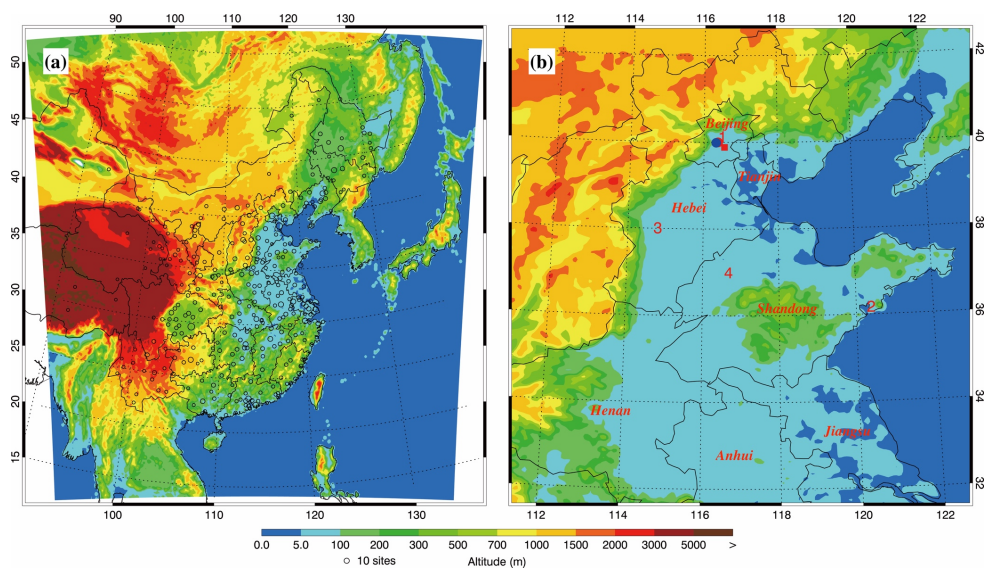
940

941

942

943

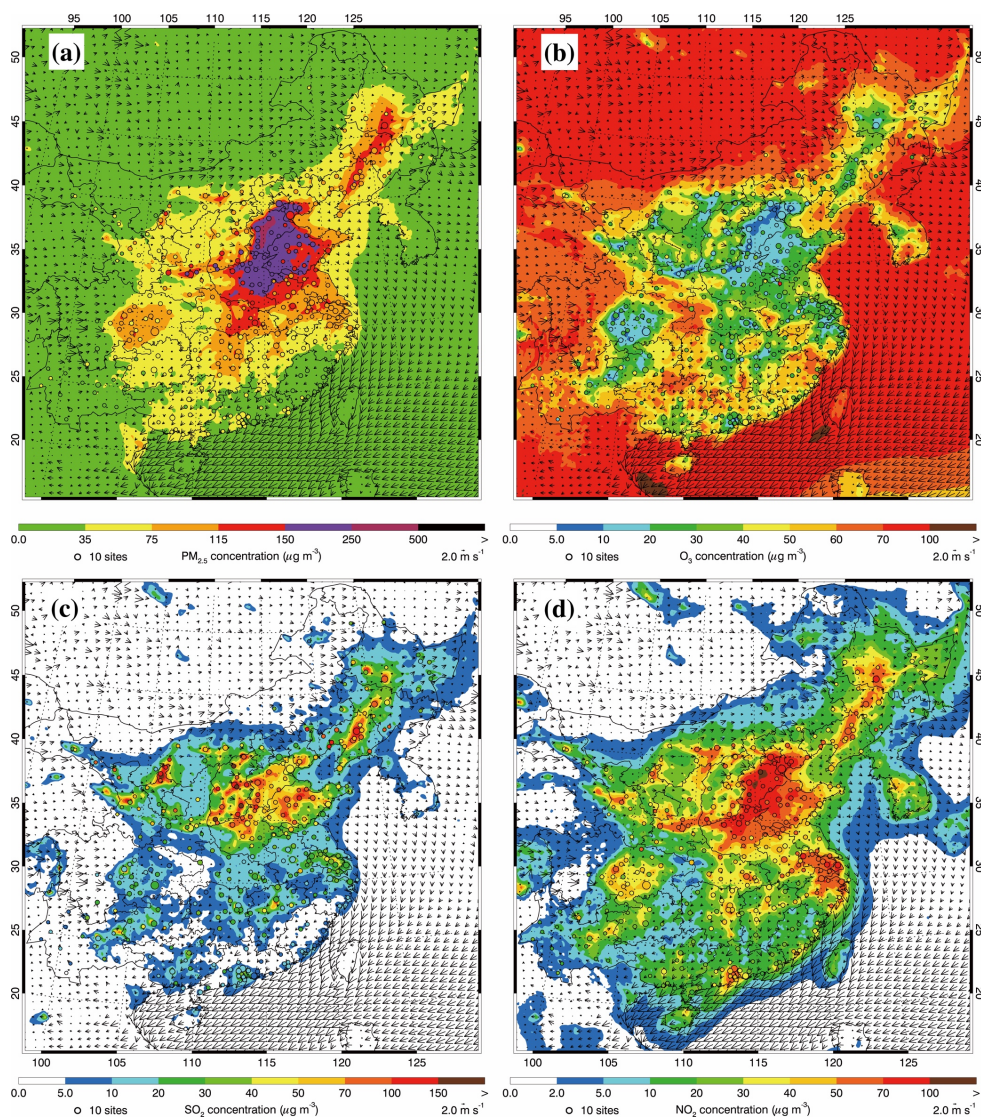
944



945
946

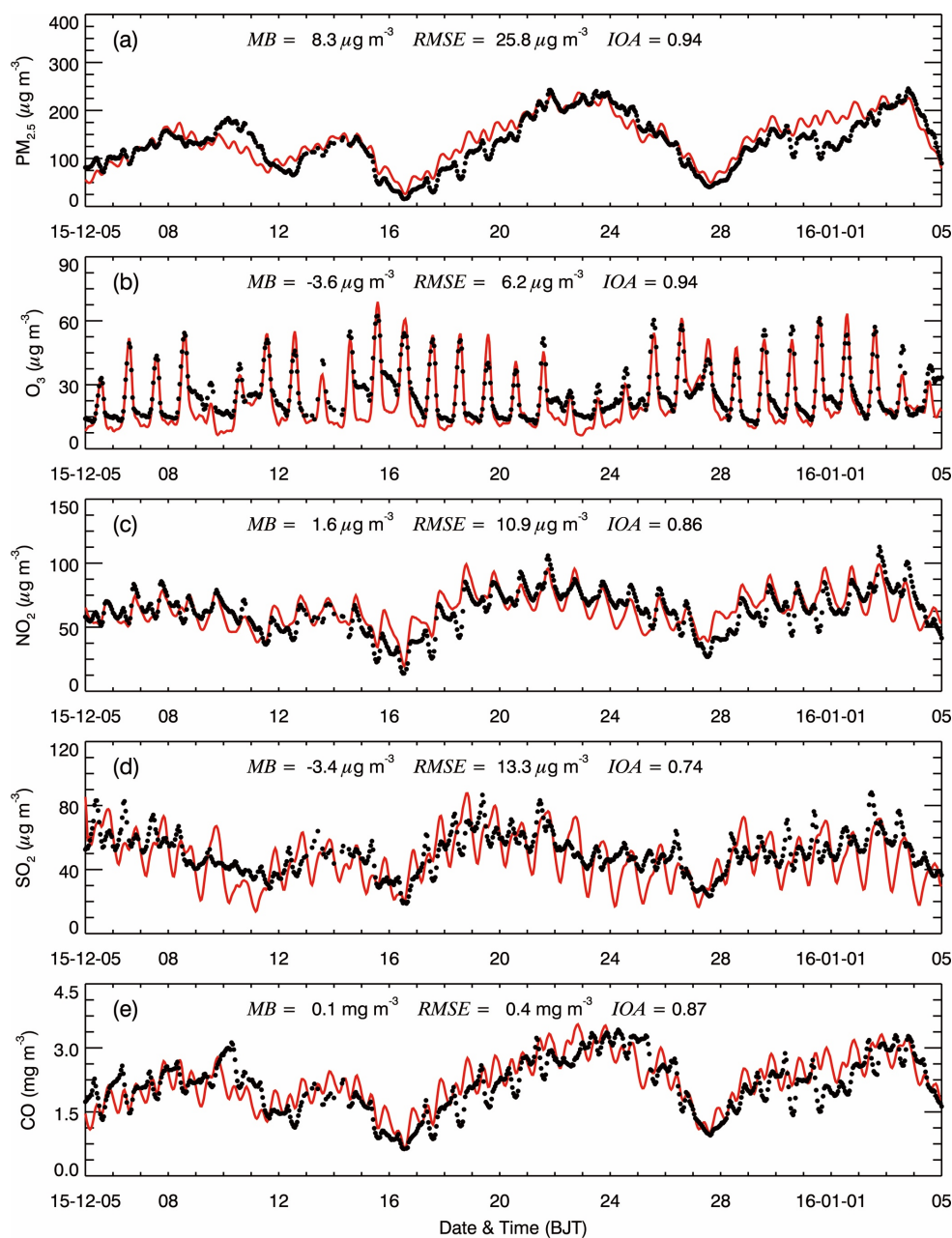
947 Figure 1 (a) WRF-CHEM simulation domain with topography and (b) North China Plain. In
948 (a), the blue circles represent centers of cities with ambient monitoring sites in, and the size
949 of blue circles denotes the number of ambient monitoring sites of cities. In (b), the blue and
950 red filled circles denote the NCNST and IRSDE site, respectively, and the red filled rectangle
951 denotes the meteorological site. The red numbers denote the CERN sites with the solar
952 radiation measurement. 1: Beijing urban; 2: Jiaozhouwan; 3: Yucheng; 4: Luancheng.

953
954
955
956
957



958
959
960
961
962
963
964
965
966
967

Figure 2 Pattern comparisons of simulated (color counters) vs. observed (colored circles) near-surface mass concentrations of (a) $PM_{2.5}$, (b) O_3 , (c) NO_2 , and (d) SO_2 averaged from 05 December 2015 to 04 January 2016. The black arrows indicate simulated surface winds.



968

969

970 Figure 3 Comparison of observed (black dots) and simulated (solid red lines) diurnal profiles

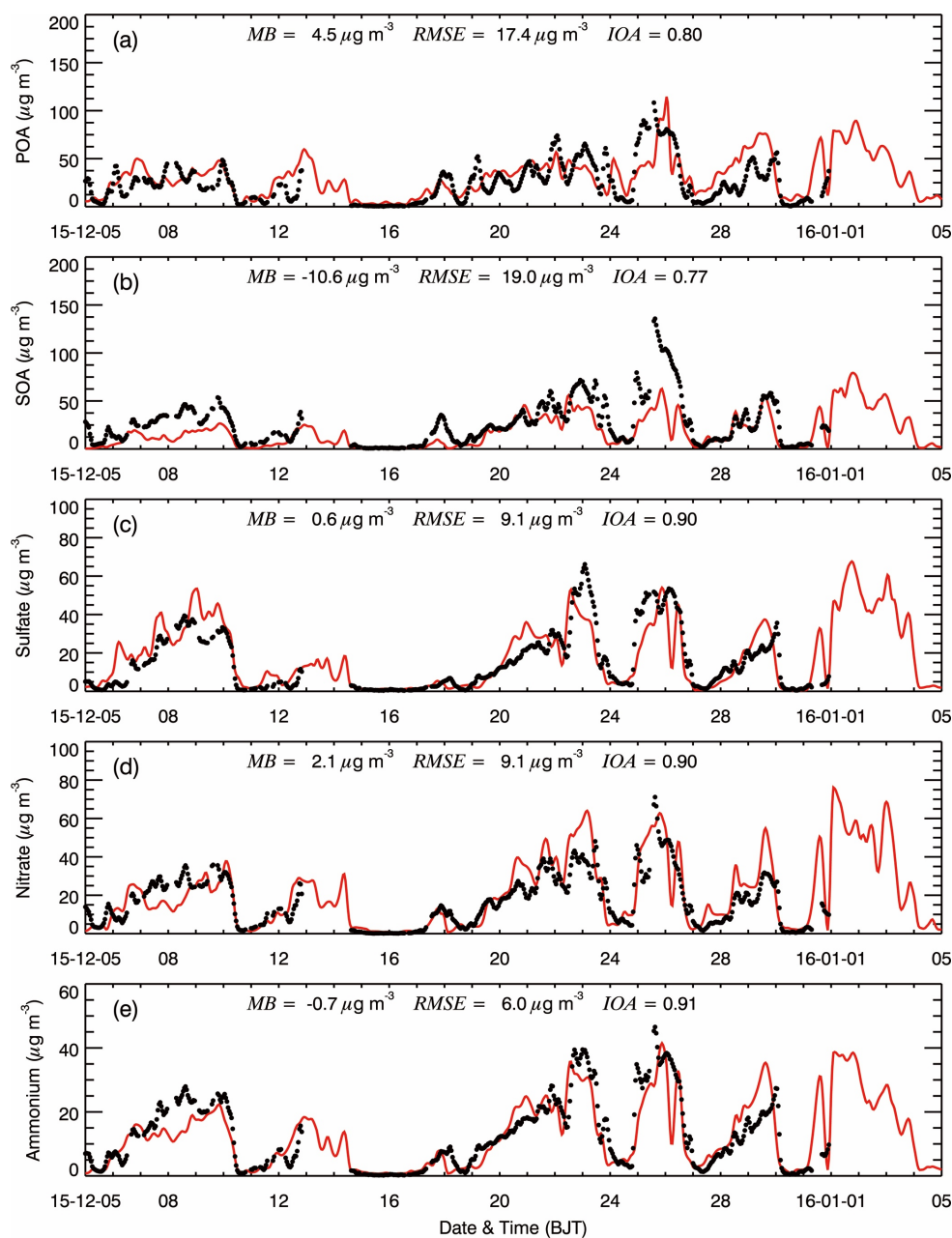
971 of near-surface hourly mass concentrations of (a) $\text{PM}_{2.5}$, (b) O_3 , (c) NO_2 , (d) SO_2 , and (d) CO

972 averaged at monitoring sites in NCP from 05 December 2015 to 04 January 2016.

973

974

975



976

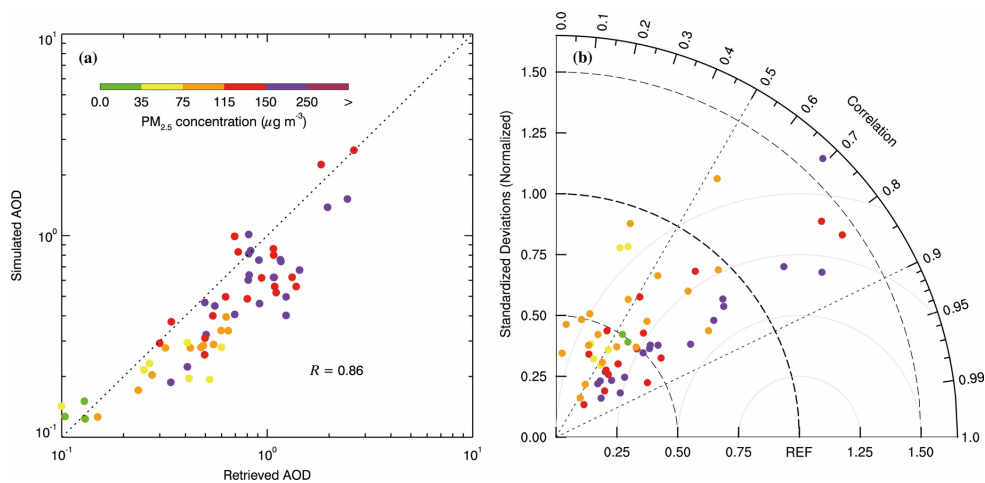
977

978 Figure 4 Comparison of measured (black dots) and simulated (black line) diurnal profiles of
979 submicron aerosol species of (a) POA, (b) SOA, (c) sulfate, (d) nitrate, and (e) ammonium at
980 NCNST site in Beijing from 05 December 2015 to 04 January 2016.

981

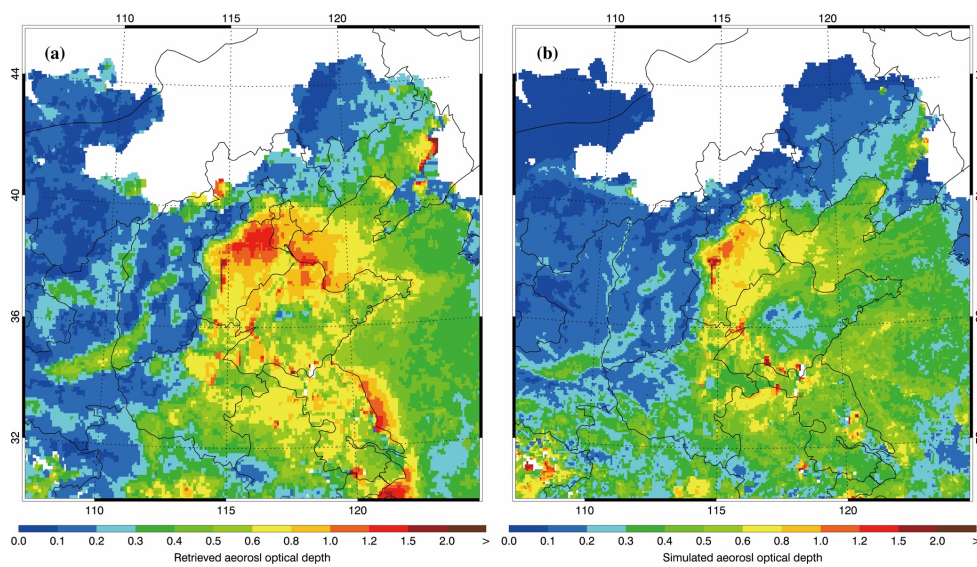
982

983



984
985
986
987
988
989
990
991
992
993

Figure 5 (a) Scatter plot of the MODIS retrieved and simulated daily AOD, (b) Taylor diagram (Taylor, 2001) to present the variance, bias and correlation of the retrieved and simulated daily AOD averaged in NCP from 05 December 2015 to 04 January 2016.



994

995

996 Figure 6 Spatial distribution of (a) retrieved and (b) simulated AOD averaged from 05
997 December 2015 to 04 January 2016 in NCP.

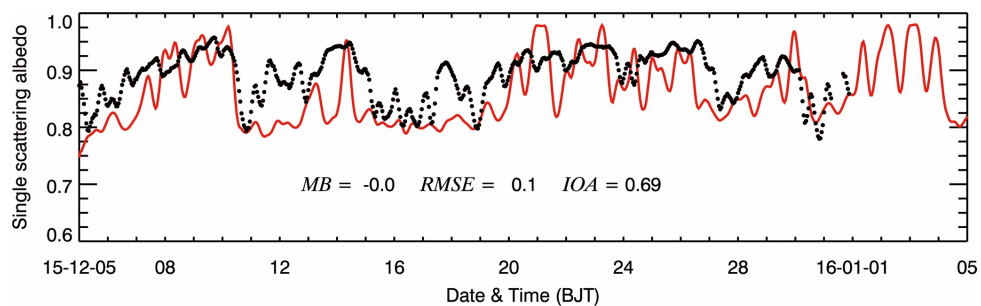
998

999

1000

1001

1002



1003

1004

1005 Figure 7 Comparison of measured (black dots) and predicted (red line) diurnal profiles of

1006 SSA in Beijing from 05 December 2015 to 04 January 2016.

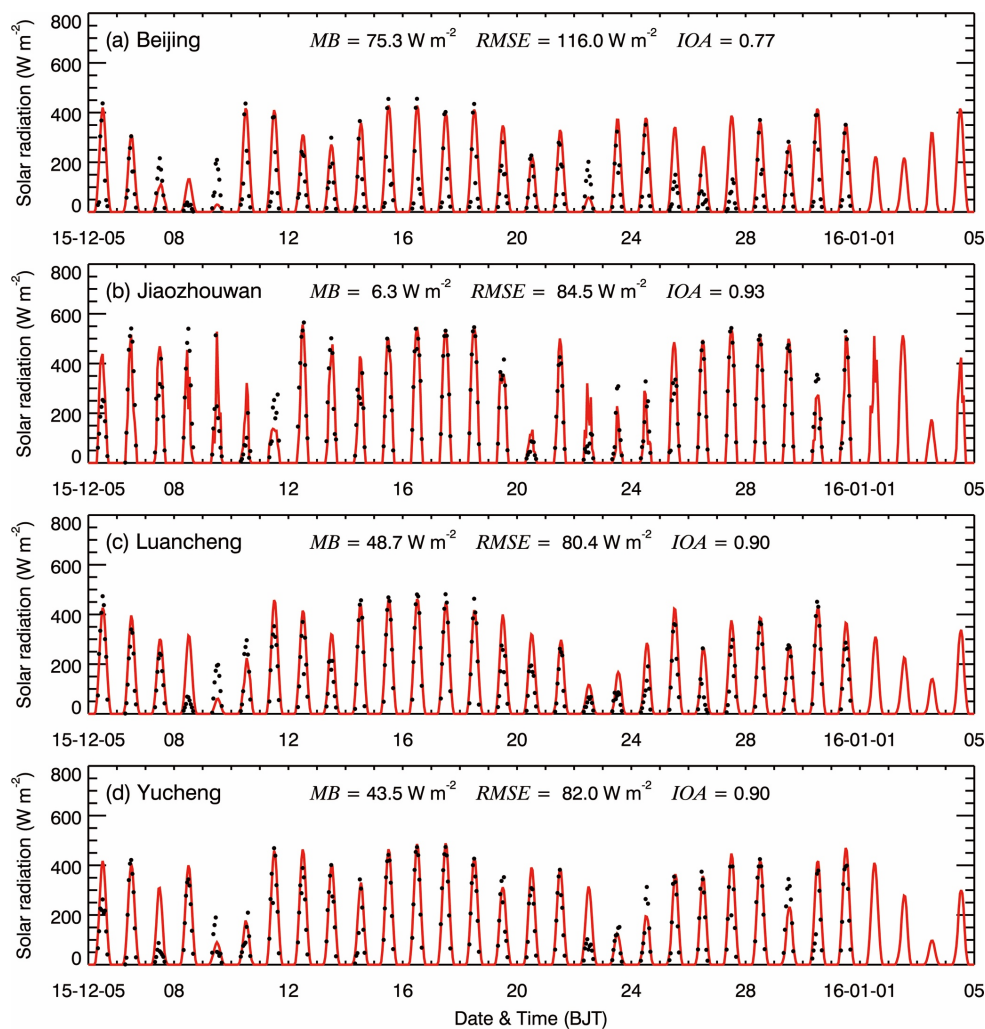
1007

1008

1009

1010

1011



1012

1013

1014 Figure 8 Comparison of measured (black dots) and predicted (red line) diurnal profiles of the
1015 SWDOWN reaching the ground surface in (a) Beijing, (b) Jiaozhouwan, (c) Luancheng, and
1016 (d) Yucheng from 05 December 2015 to 04 January 2016.

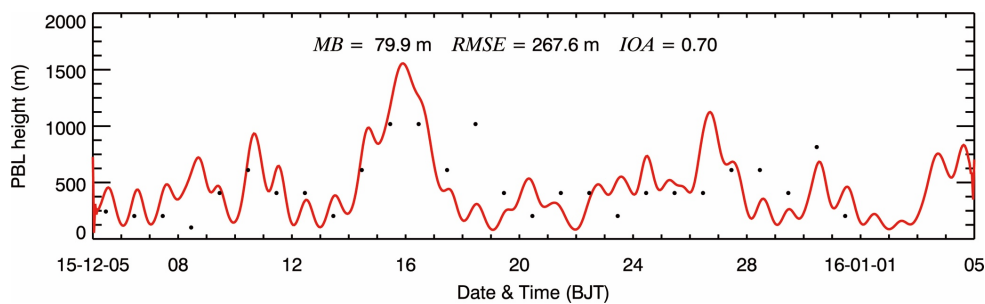
1017

1018

1019

1020

1021



1022

1023

1024 Figure 9 Comparison of predicted diurnal profile (red line) of PBLH from 05 December 2015

1025 to 04 January 2016 with observations at 12:00 BJT in Beijing.

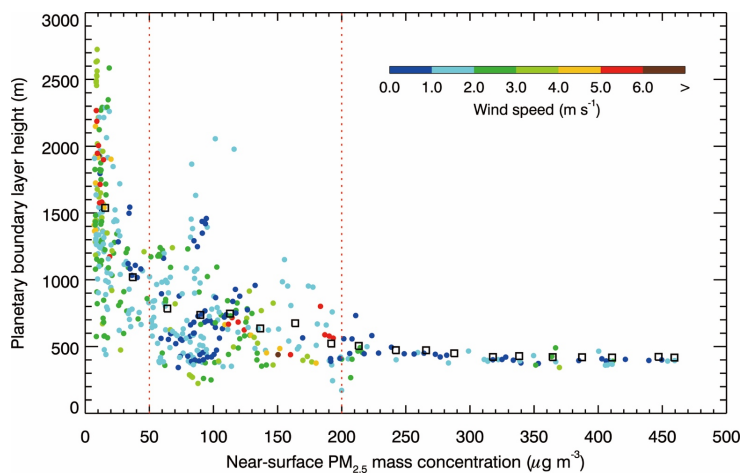
1026

1027

1028

1029

1030



1031

1032

1033 Figure 10 Scatter plot of the PBLH and near-surface $[PM_{2.5}]$ at IRSDE site from 12 January

1034 to 20 February 2014. The black rectangle shows the bin average of PBLH. The color of the

1035 filled circles denotes the WSPD at the meteorological site close to IRSDE in Figure 1b.

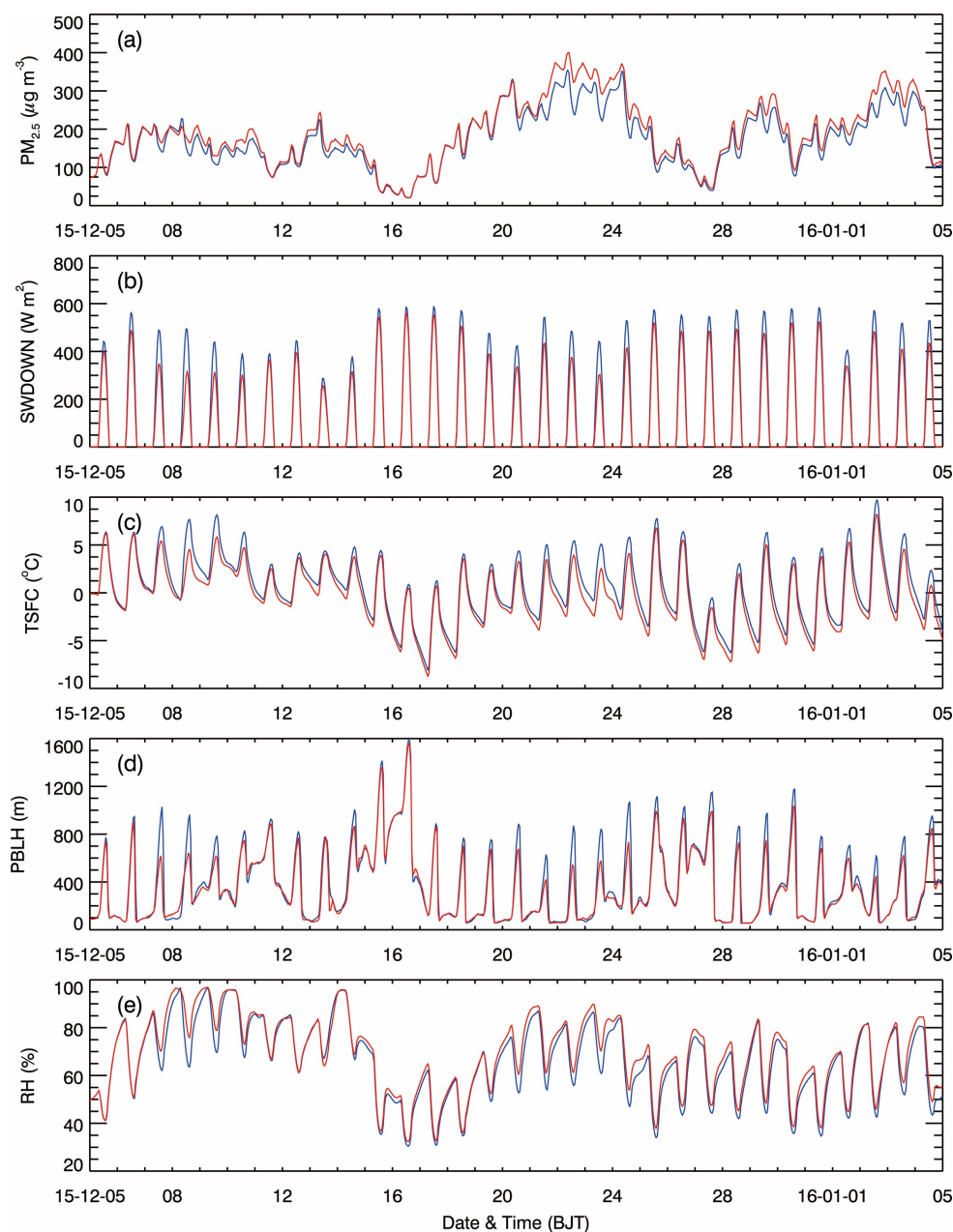
1036

1037

1038

1039

1040



1041

1042

1043 Figure 11 Temporal variations of the average (a) near-surface $[\text{PM}_{2.5}]$, (b) SWDOWN at the

1044 ground surface, (c) TSFC, (d) PBLH, and (e) RH in the most polluted area in NCP with

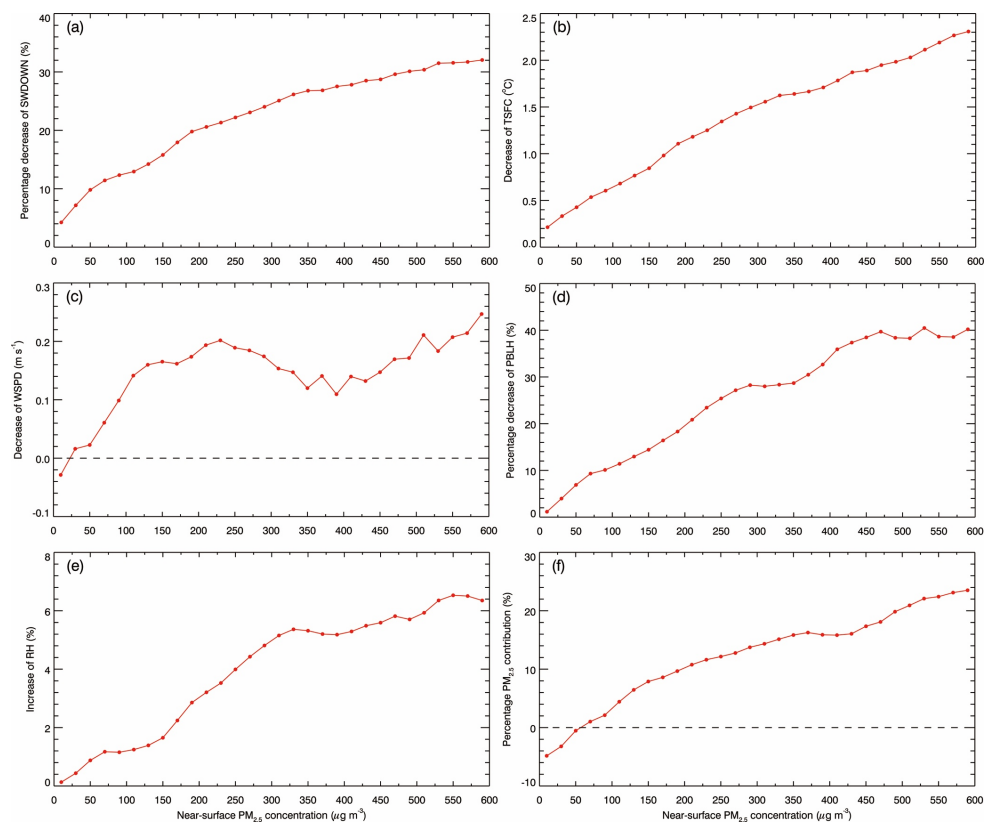
1045 $[\text{PM}_{2.5}]$ of more than $150 \mu\text{g m}^{-3}$ in f_{base} (red solid line) and f_{rad0} (blue solid line) from 05

1046 December 2015 to 04 January 2016.

1047

1048

1049



1050

1051

1052 Figure 12 Average (a) percentage decrease of SWDOWN at the ground surface, (b) decrease
1053 of TSFC, (c) decrease of WSPD, (d) percentage decrease of PBLH, (e) increase of RH, and (f)
1054 percentage contribution of near-surface $[PM_{2.5}]$ caused by the ARF, as a function of the
1055 near-surface $[PM_{2.5}]$ in NCP during daytime from 05 December 2015 to 04 January 2016.

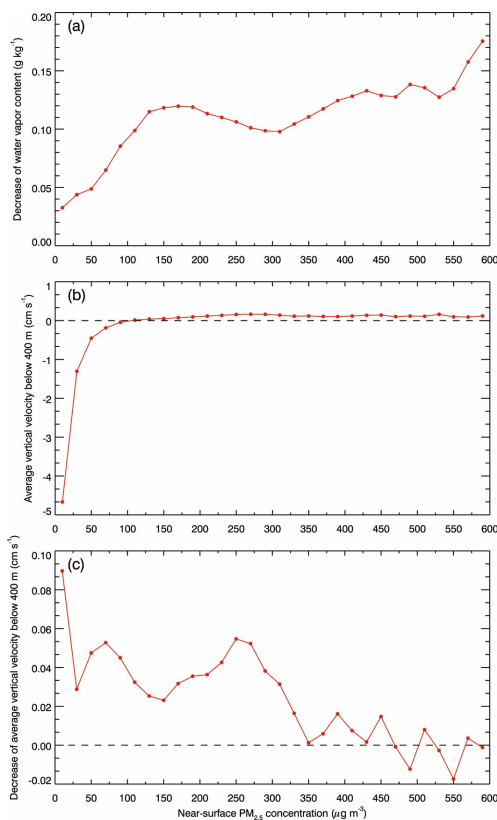
1056

1057

1058

1059

1060



1061

1062

1063 Figure 13 Average (a) decrease of water vapor content and (c) increase of average vertical
 1064 average vertical velocity below 400 m caused by the ARF, and (b) average vertical velocity below 400 m as a
 1065 function of the near-surface $[PM_{2.5}]$ in NCP during daytime from 05 December 2015 to 04
 1066 January 2016.

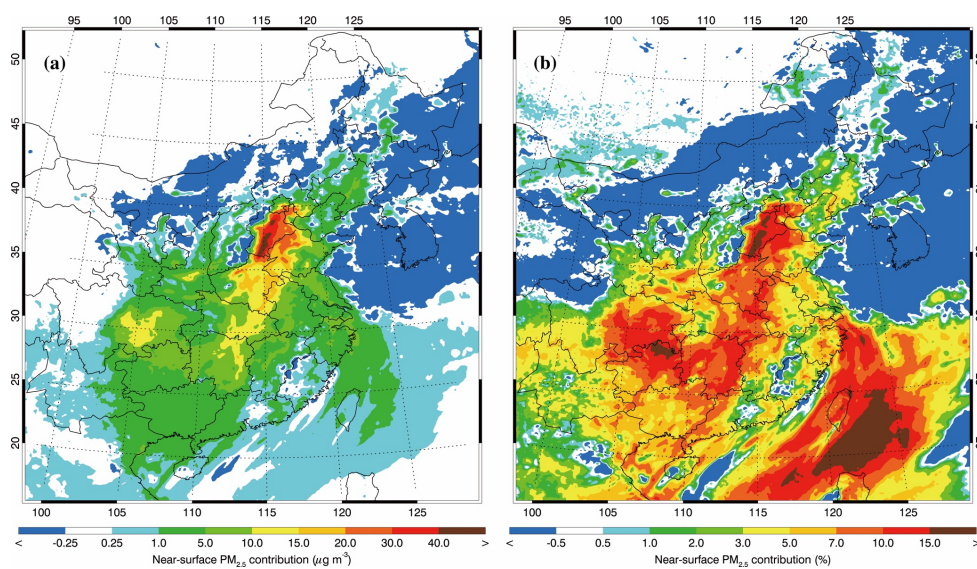
1067

1068

1069

1070

1071



1072

1073

1074 Figure 14 Near-surface $[PM_{2.5}]$ contribution caused by the ARF, averaged from 05 December
1075 2015 to 04 January 2016 in NCP.

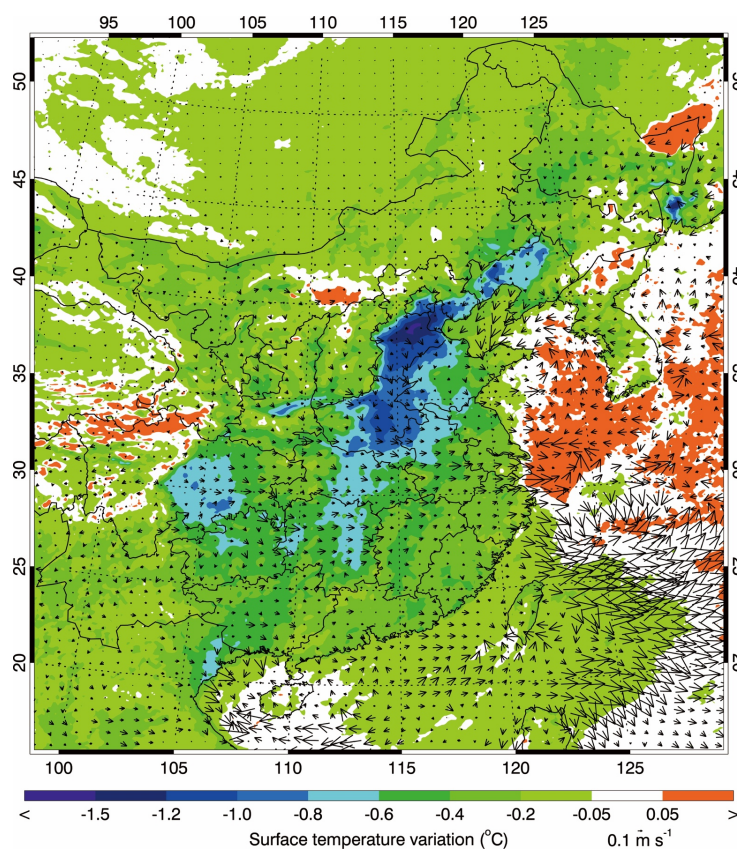
1076

1077

1078

1079

1080



1081
1082
1083
1084
1085
1086
1087
1088

Figure 15 TSFC and wind field variations caused by the ARF, averaged from 05 December 2015 to 04 January 2016 in NCP.